JCB Journal of Cell Biology

ARTICLE

Local monomer levels and established filaments potentiate non-muscle myosin 2 assembly

Melissa A. Quintanilla[1], Hiral Patel[1], Huini Wu[1], Kem A. Sochacki[2], Shreya Chandrasekar[1], Matthew Akamatsu[3], Jeremy D. Rotty[4], Farida Korobova[5], James E. Bear[6], Justin W. Taraska[2], Patrick W. Oakes[1], and Jordan R. Beach[1]

The ability to dynamically assemble contractile networks is required throughout cell physiology, yet direct biophysical mechanisms regulating non-muscle myosin 2 filament assembly in living cells are lacking. Here, we use a suite of dynamic, quantitative imaging approaches to identify deterministic factors that drive myosin filament appearance and amplification. We find that actin dynamics regulate myosin assembly, but that the static actin architecture plays a less clear role. Instead, remodeling of actin networks modulates the local myosin monomer levels and facilitates assembly through myosin:myosin-driven interactions. Using optogenetically controlled myosin, we demonstrate that locally concentrating myosin is sufficient to both form filaments and jump-start filament amplification and partitioning. By counting myosin monomers within filaments, we demonstrate a myosin-facilitated assembly process that establishes filament stacks prior to partitioning into clusters that feed higher-order networks. Together, these findings establish the biophysical mechanisms regulating the assembly of non-muscle contractile structures that are ubiquitous throughout cell biology.

Introduction

Non-muscle myosin 2 (NM2) is a cytoskeletal motor protein that builds bipolar filaments to engage actin filaments and generate contractile forces. The magnitude and orientation of these forces are highly tunable to regulate processes at the cell, tissue, and organism level (Quintanilla et al., 2023). This adaptability across spatial and temporal scales requires active remodeling of actomyosin networks. Delineating the spatiotemporal mechanisms for how cells build force-producing units is therefore critical.

NM2 filaments are dynamically assembled from NM2 monomers, which consist of two myosin heavy chains (MHC), two essential light chains, and two regulatory light chains (RLC). Each MHC consists of an N-terminal motor domain, a light chain-binding neck region, and a C-terminal alpha helix which dimerizes into a coiled-coil tail. The standard monomer-to-filament model of NM2 filament assembly begins with phosphorylation of RLC on Thr18/Ser19 (Adelstein and Conti, 1975), which drives the NM2 monomer from the folded, inactive 10S state to the unfolded, assembly-competent 6S state (Craig et al., 1983; Kendrick-Jones et al., 1987). Once unfolded, the coiled-coil tails readily associate in parallel and anti-parallel orientations to form a bipolar filament (Niederman and Pollard, 1975). Kinases from a variety of signaling networks phosphorylate the RLC to enhance NM2 filament assembly, with the dominant kinases being RhoA-activated Rho-associated coiled-coil kinase (ROCK1/2) and Ca^{++}/calmodulin-activated myosin light chain kinase (MLCK) (Totsukawa et al., 2000). In addition to phosphomodulation, in vitro studies demonstrated that NM2 filament assembly was enhanced in the presence of actin filaments (Applegate and Pardee, 1992; Mahajan and Pardee, 1996), suggesting combinatorial contributions from both kinase signaling and actin networks.

To explore molecular details of NM2 filament assembly in living cells, it is important to capture data at the length and time scales of the interactions in question. Recent advances in light microscopy have provided the spatial resolution required to observe discrete NM2 filaments (~300 nm in length) with the temporal resolution required to observe network assembly (Beach et al., 2017; Fenix et al., 2016). These studies have added dynamic mechanistic insight to earlier static electron microscopy (EM) experiments (Svitkina et al., 1989; Verkhovsky et al., 1987) and demonstrated that the simple monomer-to-filament model is incomplete in cellular contexts. More specifically, we

---

[1]Department of Cell and Molecular Physiology, Stritch School of Medicine, Loyola University Chicago, Maywood, IL, USA; [2]Laboratory of Molecular Biophysics, National Heart, Lung, and Blood Institute, National Institutes of Health, Bethesda, MD, USA; [3]Department of Biology, University of Washington, Seattle, WA, USA; [4]Department of Biochemistry, Uniformed Services University of the Health Sciences, Bethesda, MD, USA; [5]Feinberg School of Medicine, Northwestern University, Chicago, IL, USA; [6]Department of Cell Biology and Physiology, University of North Carolina-Chapel Hill, Chapel Hill, NC, USA.

Correspondence to Patrick W. Oakes: poakes@luc.edu; Jordan R. Beach: jbeach1@luc.edu.

Rockefeller University Press
J. Cell Biol. 2024 Vol. 223 No. 4 e202305023

https://doi.org/10.1083/jcb.202305023

and others observed that once an initial NM2 filament is established by unknown mechanisms in the lamella of a migrating cell, it grows in intensity and then "partitions" into a cluster of filaments or "expands" into a stack of filaments (Beach et al., 2017; Fenix et al., 2016). These clusters/stacks then merge with the higher-order actomyosin networks within the cell (stress fibers, transverse arcs, etc.). Similar progressions have been observed in contractile ring assembly (Henson et al., 2017), suggesting a common and universal mechanism for initiating and amplifying NM2 networks.

Despite these technology-enabled advances, we currently lack an experimentally supported working model for how a nascent NM2 filament is precisely established in space and time within a cell. We also do not understand how nascent NM2 filaments contribute to the higher-order network assembly required for physiological levels of contraction. Here, we show that leading edge retractions are better predictors of NM2 filament assembly than canonically proposed calcium and RhoA signaling events. Similarly, we do not observe a static actin ultrastructure that is prognostic of NM2 filament formation. Instead, we find that actin dynamics regulate NM2 filament assembly, decreasing assembly when actin dynamics are stalled and amplifying assembly following the breakdown of central and posterior actomyosin structures elsewhere in the cell. Additionally, using optogenetics, we find that by locally increasing myosin concentration, we can assemble NM2 filaments and initiate filament amplification and further partitioning. Finally, using molecular standard candles, we count the number of myosin monomers in filaments and show that monomers are more likely to add to existing myosin clusters than initiate nascent filament clusters. We also find that partitioning myosin typically already contains multiple filaments, suggesting that amplification precedes partitioning. Together these findings define biophysical mechanisms that complement biochemical signaling to modulate the dynamics of NM2 filament assembly within cells.

Results

Leading edge retractions precede nascent NM2 filament appearance

To better understand the precise events that precede nascent NM2 filament assembly—defined as the earliest frame a bipolar structure is identifiable—we initially tested the spatiotemporal correlation of filament appearance with known upstream biochemical modulators.

We used dermal mouse fibroblasts (Rotty et al., 2015) to generate a stable cell line with the N-terminus of endogenous NM2A tagged with HaloTag (Halo-NM2A) and exogenously expressed established fluorescent biosensors to localize calcium (GCaMP7s) or active RhoA (Anillin AHPH) (Dana et al., 2019; Piekny and Glotzer, 2008). We then imaged the lamella of migrating cells, where discrete NM2 assembly events can readily be observed with high-resolution light microscopy (Fig. 1 A and Video 1) (Beach et al., 2017).

Although we detected both calcium and RhoA activity in the lamella, we rarely observed either signaling cascade preceding NM2 filament appearance with any apparent precision. When imaging the calcium biosensor, occasionally, an NM2 filament appearance followed a calcium flash, but many calcium flashes did not result in filament appearances (Fig. 1 B; kymograph). Flashes also usually filled the entire lamella, arguing against a role in precise spatial control of NM2 assembly (Fig. 1 B; right panels). In contrast, active-RhoA did occasionally appear spatially coincident with NM2 filaments (Fig. 1 C). However, only a fraction of NM2 filament appearance events (~20%) were spatiotemporally preceded by discrete active-RhoA signal (Fig. 1 C; left kymograph). We observed a similar fraction of NM2 clusters with active-RhoA appearing after the NM2 filament appears (~30%), reminiscent of NM2-dependent RhoA activation observed in other systems (Priya et al., 2015). In addition, a majority of NM2 filament appearances (~50%) did not display any apparent active-RhoA signal over the background (Fig. 1 C; right kymograph). Finally, we quantified NM2 filament appearances before and after treatment with small molecule inhibitors of MLCK (peptide 18) or ROCK1/2 (Y27632; Fig. 1 D). We observed no difference in filament appearance upon inhibition of MLCK, and an increase, not decrease, in filament appearance upon inhibition of ROCK1/2. While canonical RLC kinases undoubtedly contribute to NM2 filament assembly, this imaging, perhaps due to the sensitivity of the biosensors and the experimental parameters, failed to observe robust spatiotemporal precision in RLC kinase contribution to initiate assembly events.

NM2 filaments assemble in a wide array of actin structures

We next turned to the actin architecture as a potential contributor to the spatiotemporal establishment of nascent NM2 filaments, as previous in vitro work established that filamentous actin favors NM2 filament assembly (Applegate and Pardee, 1992; Mahajan and Pardee, 1996). To better understand the lamellar actin architecture where nascent NM2 filaments are formed, we performed correlative light and electron microscopy (CLEM) (Svitkina, 2022; Svitkina and Borisy, 1998). We manually unroofed migrating GFP-NM2A fibroblasts (Fig. 1, E and F) and imaged them with both super-resolution fluorescence and platinum replica electron microscopy (PREM; Fig. 1, F–I) (Sochacki et al., 2017, 2021; Sochacki and Taraska, 2017). Within an unroofed lamella, we observed a range of fluorescent NM2A structures, from low-intensity doublets with two distinct puncta ~300 nm apart (consistent with a bipolar filament or subresolution stack; Fig. 1, G–I; arrowheads) to larger high-intensity clusters with many puncta indicating that they contain many NM2A filaments (Fig. 1, G–I; arrows). Due to the similar diameter of NM2 bipolar filaments relative to actin filaments, and the overall density of the actin cytoskeleton, we could not distinguish NM2 bipolar filaments in the PREM images, similar to previous reports (Svitkina et al., 1989). However, we could observe the local actin architecture where NM2 structures were present and not present. First, the NM2 structures exist in a diverse array of lamellar actin network architectures. This includes both seemingly disorganized actin and higher-density bundled actin. Second, while the largest NM2 clusters typically overlapped with regions of bundled actin (Fig. 1, G–I; see arrows in PREM), there were no obvious underlying actin features prognostic of low-

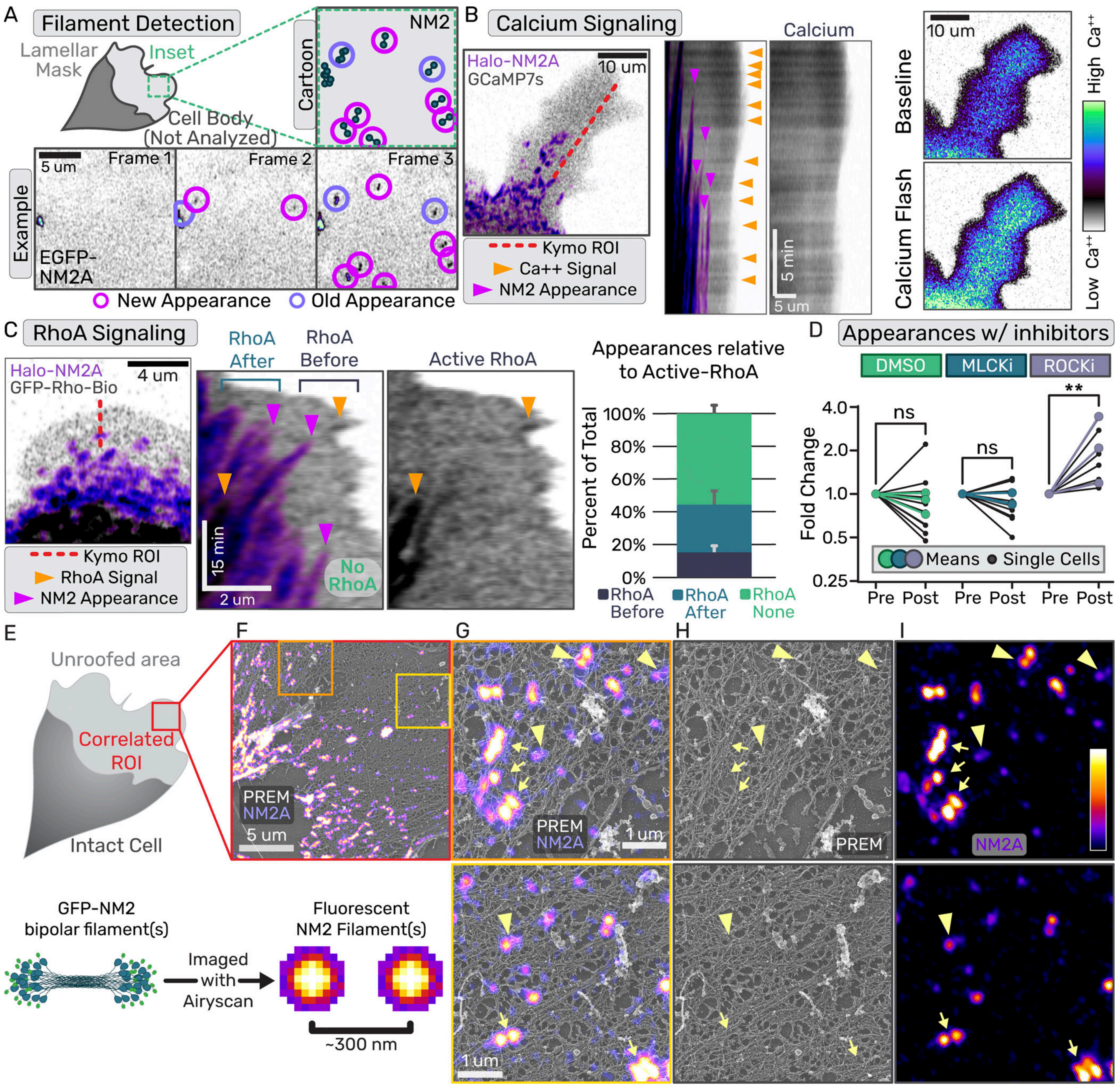

Figure 1. **Canonical signaling mechanisms do not precisely correlate with nascent NM2 filament appearances. (A)** Example of NM2 filament appearance detection workflow with both cartoon and example frames. **(B)** Confocal imaging of Halo-NM2A (purple) and GCaMP7s (inverted grey). Left panel displays an example frame with kymograph ROI indicated by the red dotted line. Middle panels display overlay kymograph or calcium-alone kymograph. Orange arrows indicate calcium sparks and magenta arrows indicate NM2 filament appearances. Right panels display the same lamella before and after a calcium flash, demonstrating the lack of spacial precision in the cytosolic calcium. **(C)** Confocal imaging of Halo-NM2A (purple) and RhoA biosensor (inverted grey). The left panel displays an example frame with kymograph ROI indicated by the red dotted line. Right panels display overlay kymograph or RhoA biosensor alone kymograph. Orange arrows indicate an active RhoA signal and magenta arrows indicate NM2 filament appearance. NM2 filaments that appear before, after, or without any RhoA signal are indicated on the left kymograph and quantified in the subsequent graph. Error bars indicate standard deviation from 395 filament appearance events from 12 cells from 4 independent experiments. **(D)** Appearance rate of NM2 filaments relative to pretreatment for control (DMSO; green), MLCK inhibition (blue), and ROCK inhibition (purple). Small circles indicate individual cells and large circles indicate experimental means from 3 independent experiments. Wilcoxon matched-pairs signed rank test performed comparing each cell. DMSO: 12 cells, MLCKi: 12 cells, ROCKi: 9 cells. P = 0.0039 for ROCKi relative to DMSO control. **(E)** The upper cartoon displays a migrating fibroblast with unroofed lamella used for correlative light and electron microscopy (CLEM). The lower cartoon depicts EGFP-NM2A in filamentous form and the fluorescent signal (fire LUT) that is detected from this structure. **(F)** Overlay of correlated platinum replica electron micrograph (PREM) and super-resolution fluorescent micrograph of EGFP-NM2A (fire LUT) in an unroofed lamella. Orange and yellow boxes indicate the zoom inset in G–I. **(G–I)** Overlay, PREM alone, or EGFP-NM2A alone zoom insets from (F). Intensity LUT is indicated to the right. Yellow arrows indicate high-intensity NM2A clusters or filaments that overlay on organized, bundled actin in PREM. Yellow arrowheads indicate low intensity NM2A doublets that overlay on disorganized actin arrays without any qualitative difference from adjacent actin regions.

intensity NM2 doublets (Fig. 1, G–I; see arrowheads in PREM), with neighboring actin regions appearing indistinguishable from NM2-containing actin regions. Therefore, while filamentous actin supports NM2 assembly and there are certainly ultrastructural details within filamentous actin that are beyond the resolution of our PREM imaging, we do not observe specific static actin architectures that might be facilitating nascent NM2 assembly events.

Actin dynamics facilitate nascent NM2 filament appearance

To identify additional factors that might dictate nascent assembly, we assessed dynamic lamellar NM2 behavior in polarized fibroblasts. Similar to previous reports (Burnette et al., 2011; Verkhovsky et al., 1995), we often find that NM2 filament appearance is preceded by a leading edge retraction (Fig. 2 A and Video 2). To more carefully observe this correlation, we imaged Halo-NM2A fibroblasts expressing EGFP-RhoBio, which acted as a cytosolic marker to enable visualization of leading-edge dynamics. Kymographs drawn through the leading edge illustrated multiple retractions of the cell edge that led to subsequent NM2 filament appearance in the lamella (Fig. 2 B). Similar results were obtained with NM2 and EGFP-VASP (Fig. S1). Quantification of this observation revealed a vast majority (~80%) of appearance events were clearly preceded by leading-edge retraction (Fig. 2 C).

To directly test the role of leading-edge retractions and actin dynamics in NM2 filament assembly, we adopted a drug cocktail consisting of jasplakinolide and latrunculin (JL) that arrests actin dynamics by inhibiting both polymerization and depolymerization (Peng et al., 2011). First, we confirmed that JL administration stalls leading edge dynamics in the fibroblasts within seconds (Fig. 2 D and Video 3). We then again quantified the rate of NM2 filament appearance in the lamella before and after pharmacological treatment. We found that the relative appearance rate did not change in cells treated with DMSO, but significantly decreased upon the addition of the actin-stalling JL cocktail (Fig. 2, E and F; and Videos 4 and 5). This demonstrates that while NM2 filament assembly can occur in their absence, leading-edge retractions and dynamic actin aid in the process.

Globally elevating NM2 monomer availability initiates filament assembly

To further explore how cytoskeletal dynamics contribute to NM2 assembly events, we performed long-term time-lapse imaging of migratory primary MEFs from EGFP-NM2A knock-in mice (Zhang et al., 2012) transduced with a lentiviral fluorescent probe for filamentous actin, FTractin-3x-mScarlet (Johnson and Schell, 2009; Yi et al., 2012). By monitoring cell morphology, NM2 assembly, and actin architectures (Video 6), we observed a qualitative correlation between NM2 filament appearance and tail retraction events (Fig. 3 A; and Video 7). This was reminiscent of previous results where ROCK inhibition with Y27632 resulted in the disassembly of central/posterior structures but enhanced growth of NM2 in the lamella (Beach et al., 2017; Chou et al., 2024). Here, we were able to recapitulate (Video 8) and quantify the effect of ROCK inhibition on lamellar filament appearance events (Fig. 1 D and Fig. 3 B). We, therefore, hypothesized that global cytosolic monomer availability in the cytoplasm, whether through changes in morphology (stress fiber disassembly upon tail retraction) or pharmacological perturbation (ROCK inhibition), regulates NM2 filament assembly. To determine if cytosolic monomer levels could drive filament assembly in the absence of actin dynamics, we treated cells simultaneously with JL and ROCK inhibitor (JLY; Fig. 3 C and Video 9) (Peng et al., 2011). This JLY treatment not only rescued the NM2 filament appearance but increased it relative to the control (Fig. 3 D). This demonstrates that a global increase in cytosolic monomer levels upon stress fiber disassembly is sufficient to initiate NM2 filament assembly, even in the absence of actin dynamics.

Locally increasing NM2 monomer concentration initiates filament assembly

To directly test if artificially enhancing local NM2 monomer levels in a cell is sufficient to initiate NM2 filament assembly independent of upstream signaling, we engineered an improved light-inducible dimer (iLID) optogenetic system to optically recruit NM2 to the cortex of migrating fibroblasts (Guntas et al., 2015). We expressed a membrane-anchored LOV2-SsrA peptide in our Halo-tagged NM2A knock-in fibroblast cell line, along with recruitable SspB-mApple-NM2A that can bind anchored SsrA upon blue light activation (Fig. 4 A). We then imaged the lamella while locally stimulating with blue light in a region devoid of NM2A filaments (Fig. 4 B and Video 10). Within minutes, the photorecruitable NM2A (blue) began accumulating in the stimulated region, followed shortly thereafter by the endogenous NM2A (purple; Fig. 4, C and D). Punctate filamentous structures containing a mixture of recruitable and endogenous NM2A continued to enrich and flow retrograde out of the stimulated region. Quantification of the activation region (orange), a region immediately downstream of retrograde flow (green), and a control lamellar region where normal NM2 filament assembly and growth occurs (yellow) demonstrate that locally increasing NM2 monomer concentration without directly increasing RLC kinase signaling is sufficient to initiate filament formation, and that established NM2 filaments can enhance local filament assembly (Fig. 4 D).

Established NM2 filaments potentiate filament assembly

Considering we could faithfully observe both NM2 filament initiating events and the enhancement of established NM2 filament clusters, we next sought to quantify their relative contributions to total lamellar filament assembly. Specifically, we asked if a new NM2 filament forms in the lamella, and what is the likelihood that filament initiates a new cluster versus building into an existing cluster. To do so, we adopted a molecular counting workflow using "standard candles" to build a standard curve of fluorescence and subsequently interpolate or extrapolate the number of NM2 monomers present in structures within the cell. We used a membrane-anchored protein nanocage that self-assembles with 60 subunits when expressed in cells (Fig. 5 A) (Akamatsu et al., 2019; Hsia et al., 2016). By using subunits with an EGFP on either one terminus (EGFP-60mer) or both termini (EGFP-120mer), we created two known standards. We created a third standard by expressing low levels of EGFP-

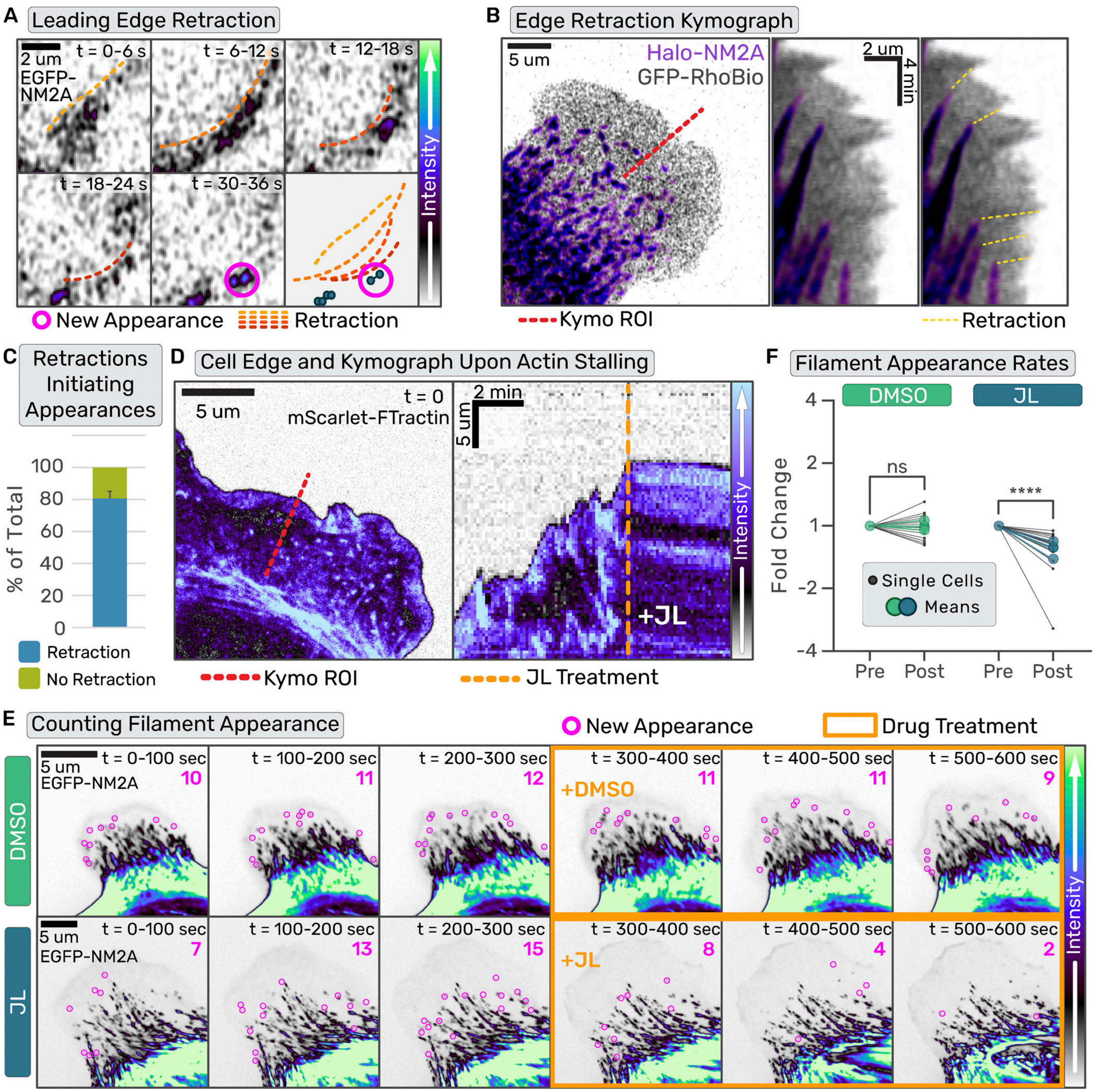

Figure 2. **Leading edge retractions initiate NM2 filament appearance events. (A)** Sum intensity projection of z-stack and three-frame time averaging for frames collected every second. Orange-to-red gradient dotted lines indicate wave-like retraction, and magenta circles indicate subsequent NM2 filament appearance. Scale bar = 2 µm. **(B)** Halo-NM2A cells transiently expressing GFP-RhoBio were imaged every second. The image is a sum intensity projection of a z-stack with NM2 in purple and RhoBio in gray. Scale bar = 10 µm. The red line indicates the ROI used for the kymograph in the right panel. Yellow dotted lines connect leading edge retractions with NM2 filament appearance. **(C)** Quantification of the number of NM2 filament appearance events preceded by (blue) or not preceded by (green) a leading edge retraction. Error bars indicate standard deviation from 395 filament appearance events from 12 cells from 4 independent experiments. **(D–F)** Confocal time series of primary EGFP-NM2A MEF cells expressing FTractin-mScarlet were acquired. For D only, the FTractin-mScarlet channel is shown and for E only, EGFP-NM2A channel is shown. **(D)** Example frame of lamellar actin (left panel) and kymograph (right panel) of lamellar dynamics pre- and post-JL treatment through the red dotted line in the left panel. The orange dotted line indicates the time of JL addition. **(E)** EGFP-NM2A images were temporally summed over 20 frames (100 s). Nascent NM2 filament appearances during that period are indicated with magenta circles and tallied in the upper right corner. Three binned time periods pre- and -post (orange outline) treatment are shown for DMSO (top row) and JL (bottom row). Scale bars = 5 µm. **(F)** Nascent NM2 filament appearance events pre- and post-treatment, normalized to pretreatment appearance events per minute, were quantified for individual cells (small black dots) and the mean of three independent experiments (large color circles). Temporal and intensity LUTs are indicated to the right. Wilcoxon matched-pairs signed rank test performed comparing each cell (DMSO: 15 cells, JL: 16 cells). P < 0.0001.

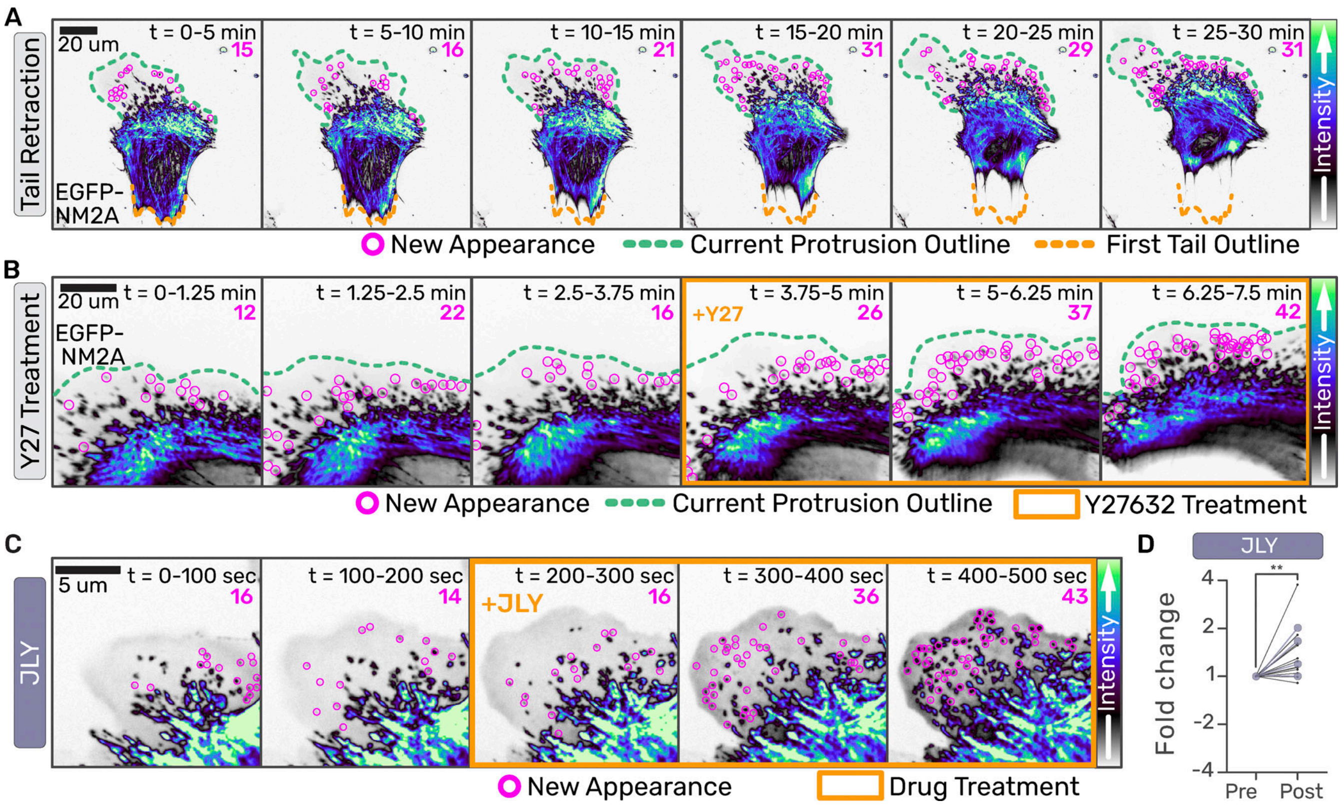

Figure 3. **Globally elevating NM2 monomer availability initiates filament assembly. (A–C)** Confocal z-stacks of primary EGFP-NM2A MEF cells were acquired. Images are sum intensity projections of z-stacks and time-sum projections of 15 frames collected every 15 s in (A) and 5 s in (B). Nascent NM2 filament appearances during that period are indicated with magenta circles and tallied in the upper right corner. The green dotted line indicates the current leading edge. The orange dotted line indicates original tail location (A) and the orange box indicates frames treated with 10 µM Y-27632 (B). Scale bars = 20 µm. (C) EGFP-NM2A sum z-projections were temporally summed over 20 frames (100 s). Nascent NM2 filament appearances during that period are indicated with magenta circles and tallied in the upper right corner. Binned time periods pre- and -post (orange box) treatment are shown for JLY treatment. Scale bar = 5 µm. Intensity LUTs are indicated to the right of each panel. **(D)** Nascent NM2 filament appearance events pre- and post-treatment were quantified, normalized to pre-treatment appearance events per minute, for individual cells (small black dots) and the mean of three independent experiments (large color circles). Wilcoxon matched-pairs signed rank test performed comparing each cell (n = 12). P = 0.0034.

actin, similar to other single-molecule actin efforts (Robin et al., 2014), such that individual fluorophores could be identified (Fig. 5 B). Each standard candle was separately expressed in fibroblasts, where we segmented and quantified the fluorescent intensity of individual candles (Fig. 5 C and Fig. S2). We then created a standard curve by plotting the mean fluorescent intensities of each standard candle as a function of the number of EGFP molecules present in the individual structures (Fig. 5 D). Fitting a line to these data demonstrated a highly linear relationship between the fluorescence intensity of a structure and the known number of EGFP molecules present.

Using identical imaging settings, we then imaged endogenous EGFP-NM2A in fibroblasts from homozygotic knock-in mice (Zhang et al., 2012). In these cells, every MHC 2A is tagged with an EGFP, and every NM2A monomer contains two EGFPs. In vitro studies and theoretical models demonstrate mature NM2A filaments consist of ∼30 monomers (Billington et al., 2013; Niederman and Pollard, 1975; Ricketson et al., 2010). Therefore, one mature NM2 filament would contain ∼60 EGFP molecules while two mature filaments would contain ∼120 EGFPs (Fig. 5 E), conveniently aligning with our known standards. Within lamellar regions (Fig. 5 F), we quantified three parameters: (1) the number of nascent NM2 filament assembly events that initiate new clusters within a given time, (2) the fluorescent intensity increase for individual clusters within the same region during the same time, and (3) the fluorescent intensity increase for all existing clusters. By converting the fluorescent intensity increase in clusters to the number of NM2 filaments using our standard curve, we could directly compare the number of nascent filament assembly events (new clusters) to the number of filaments assembling into existing clusters (Fig. 5, G and H; and Video 11).

We find that assembling NM2 is ∼100 times more likely to incorporate into existing structures than to form nascent clusters in the lamella, demonstrating the dominant contribution of NM2-facilitated assembly to the overall assembly.

NM2 structures amplify to subresolution stacks before partitioning

Provided the importance of cluster growth to total lamellar NM2 assembly and the derivation of clusters from a nascent NM2 filament, we sought to better define molecular mechanisms that enable the addition of NM2 filaments to existing structures. Previous high-resolution imaging studies observed the process

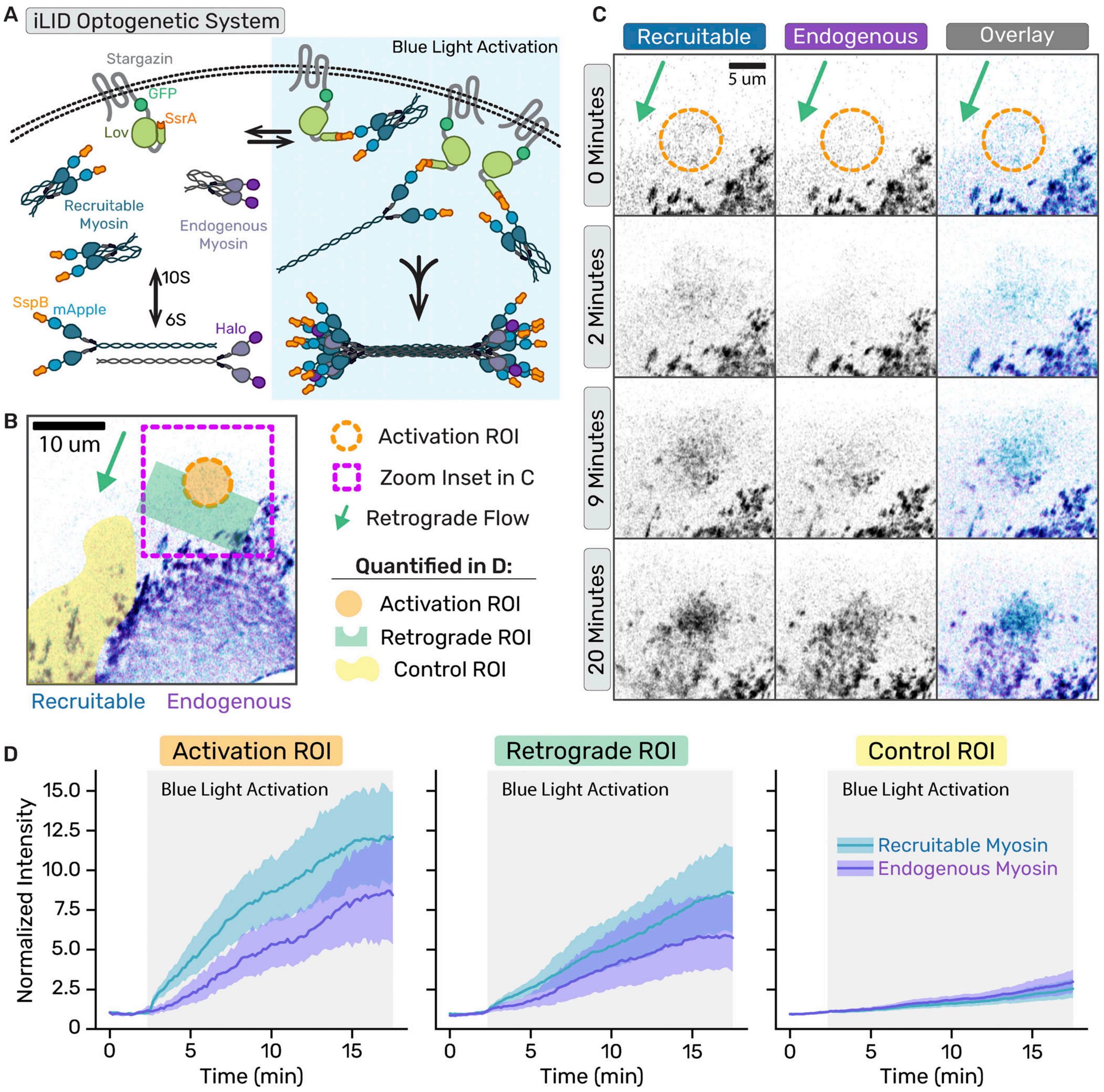

Figure 4. **Locally concentrating NM2 monomer results in filament assembly. (A)** Cartoon of iLID optogenetic system with photo-recruitable NM2 monomers expressed with endogenously tagged NM2. **(B)** Representative frame of optogenetic recruitment of NM2 monomers in the cell. **(B and C)** The magenta box indicates the zoom inset region, the orange circle marks the activated region, and the green area shows the direction of retrograde flow. **(B and D)** Activation, retrograde flow, and control areas shown in orange, green, and yellow, respectively. **(C)** Time series of optogenetic NM2 recruitment with recruitable NM2 in blue/gray and endogenous NM2 in purple/gray. The left panel is the recruitable NM2, the middle panel is endogenous, and the right panel is an overlay of the two channels. **(D)** Quantification of the normalized intensity increases (mean ± SD) upon blue light activation (gray box) in the indicated regions. The data represents 19 cells from five experiments.

by which a nascent NM2 filament grows in intensity before partitioning into multiple filamentous structures, a process that repeats sequentially to enhance cluster size as they mature into higher-order networks (Fig. 6 A) (Beach et al., 2017; Fenix et al., 2016). Two non-mutually exclusive models were proposed in which a single mature NM2 filament is partitioned into two immature filaments ("Single Filament Partitioning"), or a mature filament recruits additional monomers/filaments to establish multiple filaments prior to partitioning ("Multi-Filament Partitioning"; Fig. 6 B).

Using our molecular counting approach, we could now determine at which point during partitioning multiple NM2 filaments are present. We used both fixed and live high-resolution Airyscan imaging to resolve the number of GFP-tagged NM2

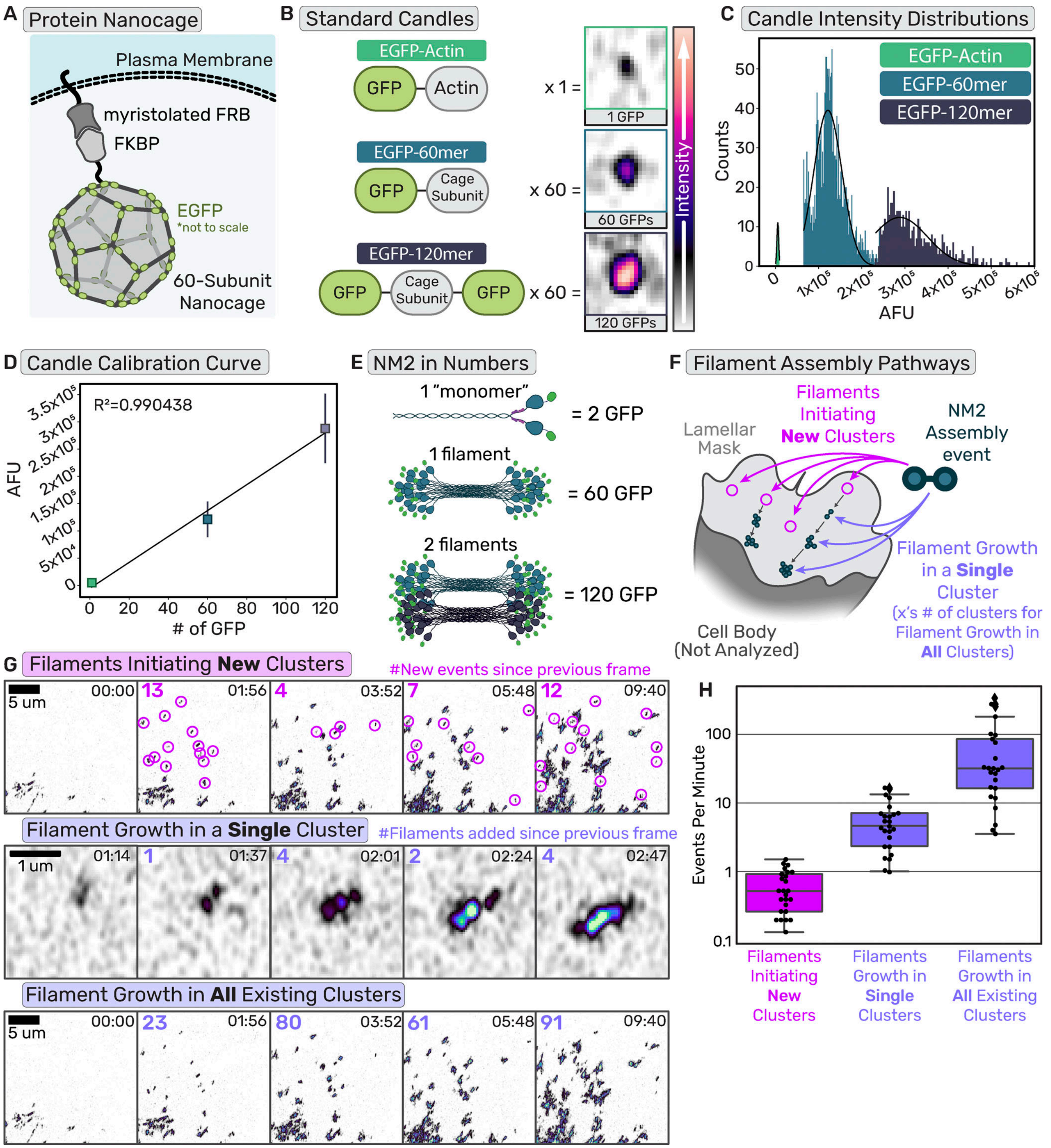

Figure 5. **Established NM2 filaments are sites of enhanced filament assembly. (A)** Cartoon of protein nanocage used as a known standard for the calibration curve. **(B)** Cartoons of the domains of the standard proteins used with the number of subunits per polymer and representative images of the standard in cells. The intensity scale bar is on the right. **(C)** Intensity histograms of the known standards with Gaussian fits. **(D)** The calibration curve was generated from the intensity distributions of the standards and the number of subunits with linear regression. *n* = 15 cells for each candle, each experimental day. **(E)** Example cartoon of NM2 monomer, filament, and filaments tagged with EGFP with the number of EGFPs in those structures. **(F)** Cartoon delineating two different NM2 filament assembly mechanisms, initiation of new clusters, or adding to existing clusters. **(G)** Example frames of cluster appearance tracking (top row), filament growth in a single cluster (middle row), and all cluster growth (bottom row), with the number of events/filaments added since the previous frame displayed upper left corner of each panel. Scale bar = 5 µm; 300 nm. **(H)** Quantification of cluster appearance rates compared with NM2 filament growth rates. Data are presented as standard box plots with median, first and third quartiles, and min and max indicated. *n* = 26 cells from three independent experiments.

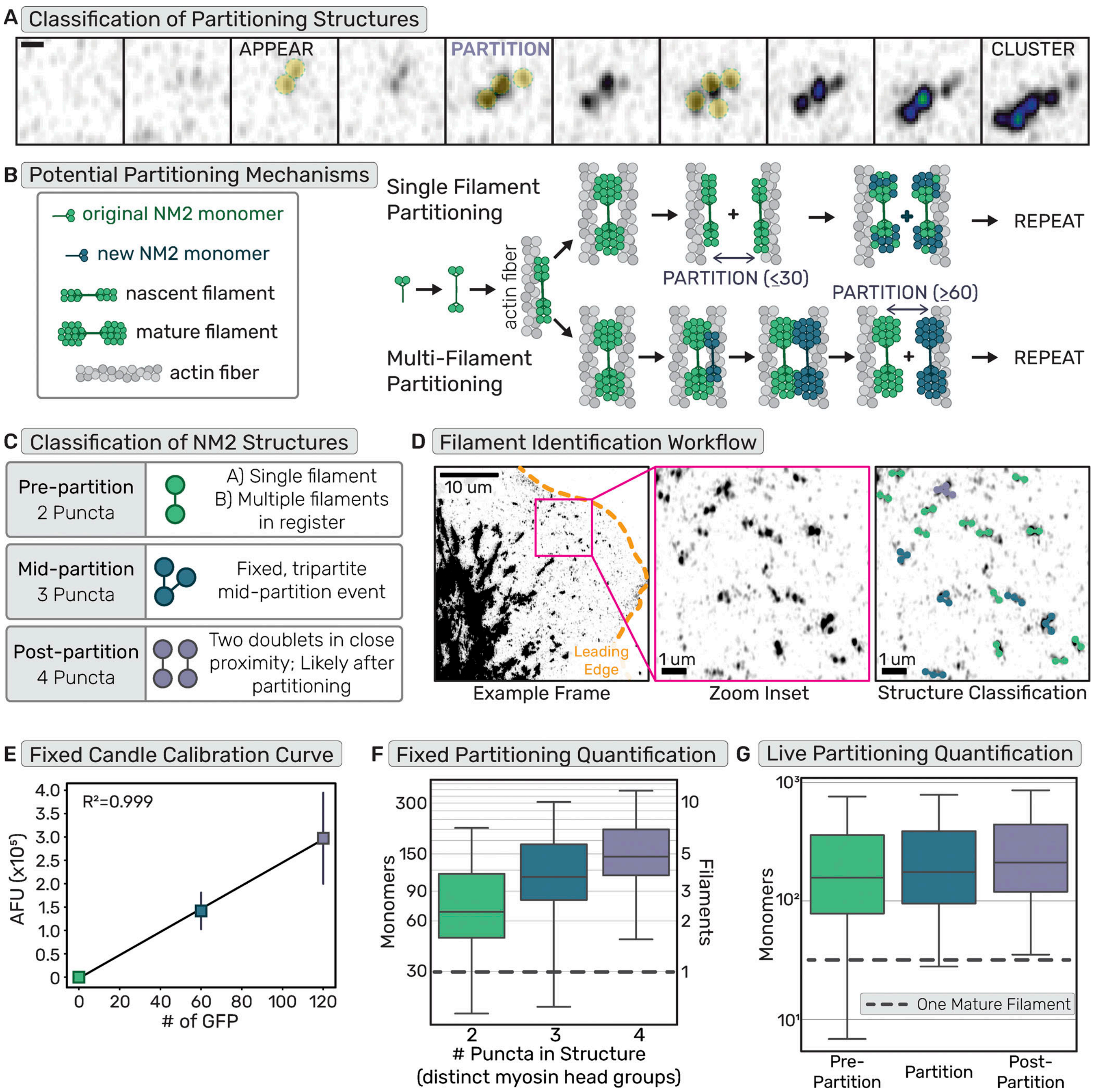

Figure 6. **NM2 structures amplify to sub-resolution stacks before partitioning. (A)** Example frames of EGFP-NM2A filament appearance, partitioning, and cluster growth. Scale bar = 300 nm. **(B)** Cartoon depicting two non-exclusive mechanisms of NM2 partitioning, containing either single or multiple filaments. **(C)** Classification of single time-point or fixed frames of NM2 fluorescent structures grouping structures based on the number of peaks/puncta and assigning them to stages of partitioning. **(D)** EGFP-NM2A sum projection example frame (left) with a leading edge outlined in orange and zoom inset in magenta. Scale bar = 10 µm. Zoom inset (middle). Scale bar = 1 µm. Zoom inset overlay (right) displays detected NM2 filaments color-coded into classes based on the number of detected puncta in the fluorescent structures. Scale bar = 1 µm. **(E)** Example calibration curve for a fixed molecular counting data set with linear regression. *n* = 15 cells for each candle, each experimental day. **(F)** Fixed NM2 partitioning results with a gray dotted line to indicate a single mature NM2 filament. *n* = 45 cells over three experiments. **(G)** Live NM2 partitioning results with a gray dotted line to indicate a single mature NM2 filament. *n* = 26 cells over three experiments. Data for (F and G) presented as standard box plots with median, first and third quartiles, and min and max indicated.

head groups within a structure. For fixed imaging experiments, we classified two-puncta bipolar structures as pre-partitioning, three-puncta structures as mid-partitioning, and four puncta structures as post-partitioning (Fig. 6, C and D; and Video 12). The identified two-puncta structures could include structures just prior to partitioning but also more nascent bipolar structures. Surprisingly, the vast majority of these two puncta structures already contained multiple NM2 filaments (Fig. 6, E and F). This suggests a rapid amplification into small sarcomeric filament stacks prior to spatial segregation of the NM2 filaments.

We paralleled this fixed data with live-cell imaging. This afforded the opportunity to isolate the exact frame prior to partitioning for each identified structure. Similar to the fixed results, most of the pre-partition or two puncta data contained multiple NM2 filaments (Fig. 6 G). This number appeared to increase upon detectable partitioning and post-partitioning states (Fig. 6 G). The higher number of NM2 monomers counted in the pre-partition data for the live experiment compared with the fixed experiment is likely due to our ability to identify partitioning events live and therefore filter out the more nascent two puncta structures that were not yet partitioned. These data demonstrate that optically resolved two-puncta structures which have previously been suggested as single NM2 filaments (Beach et al., 2014), are actually stacks of filaments in register. Notably, placing EM-guided filaments (Billington et al., 2013; Shutova et al., 2014) within the voxels from our fluorescent imaging reveals that the number of filaments we quantify within our two-puncta structures is entirely feasible (Fig. S3). Partitioning is thus the separation of multiple NM2 filaments from one another, as opposed to the splitting of a single mature filament.

Discussion

The demand for local force generation in numerous myosin 2-dependent processes dictates that NM2 filament assembly and amplification are dependent on their local environment. Canonically, it has been established that RLC phosphorylation drives the conversion of folded, inactive 10S monomers into unfolded, assembly-competent 6S monomers that can engage one another to drive nascent filament formation or incorporate into established filaments (Fig. 7 B). Our data presented here indicates an additional critical role for biophysical mechanisms in filament assembly. First, we posit that in addition to RLC kinases locally enriching 6S monomer, increases in the total cytosolic concentration of NM2 monomer (6S and 10S) increase the likelihood that sufficient monomers will dwell in a given area long enough to interact and produce a stable but immature NM2 filament (Fig. 7 C). While lower cytosolic concentrations of the RLC-phosphorylated 6S monomer are required to surpass a filament formation threshold and establish a nascent filament, higher cytosolic concentrations of non-phosphorylated 10S monomer could also surpass a filament formation threshold. Indeed, in vitro studies have demonstrated that non-phosphorylated monomers can still form filaments, albeit it at ∼15-fold higher concentrations than RLC-phosphorylated 6S monomer (Kendrick-Jones et al., 1987). Second, we introduce a biophysical component in which local NM2 monomer enrichment can be achieved strictly through dynamic reorganization of the actin cytoskeleton. In our lamellar model system, this presents as locally concentrating NM2 monomer via the retraction/collapse of leading edge protrusions (Fig. 7 D). We propose that at least three mechanisms (RLC-P 10S-6S conversion, increasing cytosolic monomer, and locally concentrating monomer) are simultaneously and collectively coordinating nascent NM2 filament assembly (Fig. 7, A–D).

Once a nascent filament is established, we find it acts as a site of enhanced assembly, suggesting that myosin:myosin interactions are the main drivers of NM2 amplification processes (Fig. 7, E and F). This amplification produces sarcomeric filament stacks and filament clusters (Fig. 7 G) that continue to spatially segregate or partition (Fig. 7 G), creating additional local assembly sites that further perpetuate and aid the amplification and generation of force (Fig. 7, H and I). We speculate that filament clusters and stack formation are driven primarily by myosin:actin interactions, with actin filament dynamics dictating stack versus cluster formation. Specifically, NM2 filaments bound to actin filaments that move apart in a parallel manner will likely remain in register with one another, allowing the NM2 filaments to generate a sarcomeric stack, while NM2 filaments bound to actin filaments that move apart in a non-parallel or disordered manner will follow suit to generate a less organized cluster. Below, we discuss and speculate on additional details of this encompassing mechanistic model.

This dependence on actin is consistent with previous reports that have highlighted myosin acting as both a motor and a crosslinker (Laevsky and Knecht, 2003). In vitro, theoretical, and cellular studies have shown that the presence of filamentous actin enhances NM2 filament assembly (Applegate and Pardee, 1992; Chou et al., 2024, *Preprint*; Grewe and Schwarz, 2020; Mahajan and Pardee, 1996). More recent cellular studies have reported actin-dependent roles in NM2 filament alignment, expansion, and partitioning (Beach et al., 2017; Fenix et al., 2016; Shutova et al., 2014). In addition, static properties of filamentous actin (bundling, twist, tension, etc.) cannot be overlooked in impacting NM2 binding and NM2 filament assembly dynamics (Hirakawa et al., 2017; Uyeda et al., 2011). Here, we build on this perspective to show that actin dynamics are critical for influencing NM2 assembly. Our observations that leading edge and tail retractions precipitate NM2 filament formation suggest a role for the rearrangement of the actin cytoskeleton in modulating NM2 monomer concentration. Specifically, we speculate that leading edge retractions (driven by actin stalling, membrane tension, posterior myosin 2 contractility, etc. [Gauthier et al., 2012; Ji et al., 2008; Nickaeen et al., 2017]) serve to locally concentrate myosin monomers by reducing the local actin pore size (Bieling et al., 2016), similar to other models for actin-dependent restricted diffusion (Andrews et al., 2008; Millius et al., 2012). In addition to a reduced physical space, the increase in actin density would facilitate local NM2 retention by acting as a kinetic trap, providing a plethora of binding sites for free monomers to interact with. This model is not exclusive to NM2, as other actin-binding proteins should be subject to the same entrapment depending on their actin-binding kinetics. The ideal NM2 monomer to engage this dynamic actin is the RLC-phosphorylated 6S monomer. However, even the inactive, folded monomer (10S) can bind actin, albeit with reduced affinity (Greene and Sellers, 1987; Ikebe and Hartshorne, 1986; Sellers, 1985), and could be enriched in an actin kinetic trap. Importantly, considering the potential for 10S monomer to both bind actin and build filaments, we suggest that the cytosolic levels of available 10S monomer without RLC phosphorylation may be directly contributing to filament formation, in addition to the canonical model of an indirect contribution via supplying RLC kinases to produce the assembly-competent 6S monomers. This

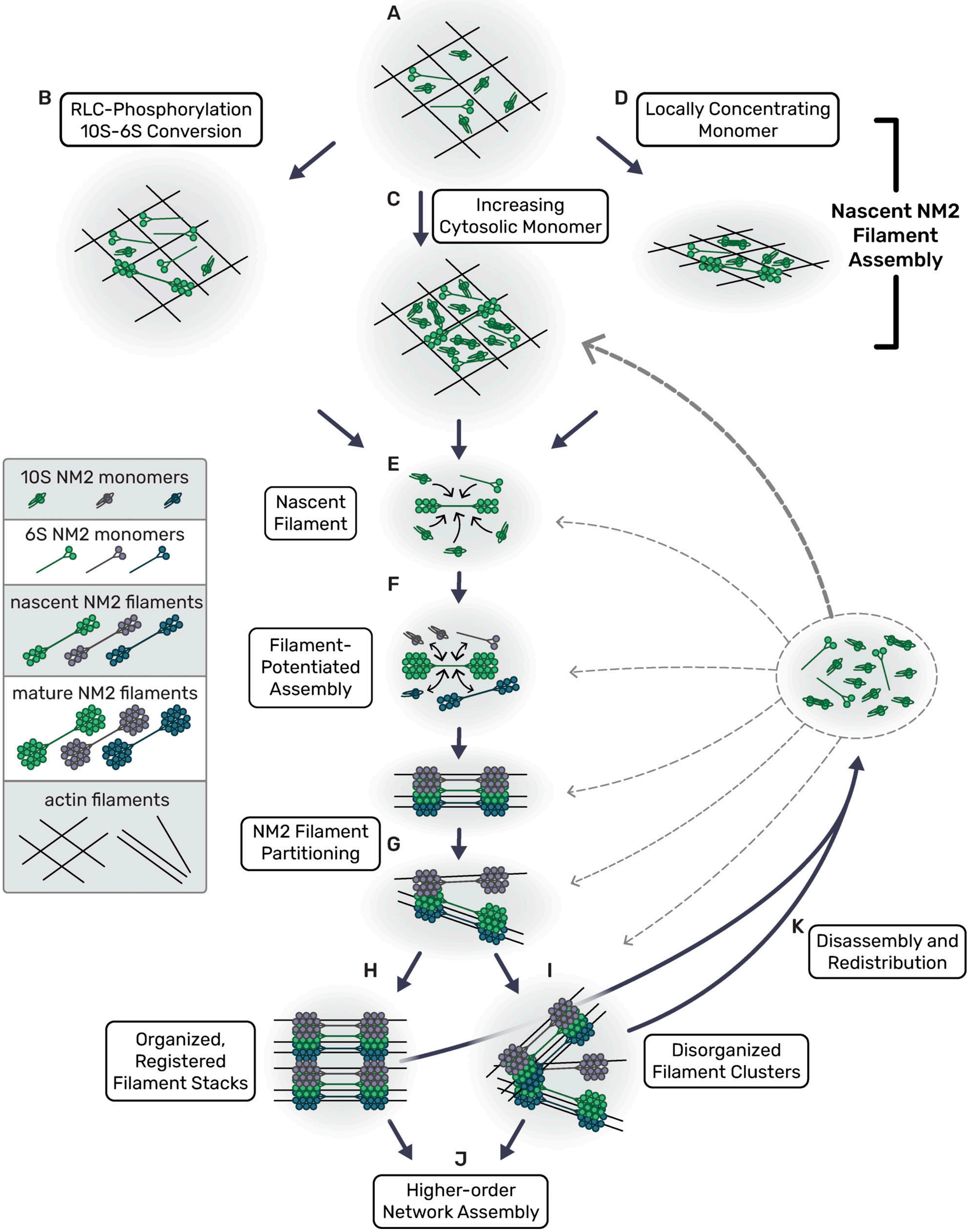

Figure 7. **Model for NM2 filament assembly in cells. (A)** Cytosolic myosin monomers in the actin network; large pore size in actin "net." **(B–D)** Three non-mutually exclusive mechanisms for nascent filament assembly. **(B)** RLC kinases drive conversion from folded 10S to unfolded assembly-competent 6S monomers. **(C)** Cytosolic myosin monomer concentration increases from NM2 filament turnover in other areas of the cell. **(D)** Retraction collapses actin network, increases monomer density, and potentiates NM2 filament assembly. **(E)** Local monomers add to nascent NM2 filament until it becomes a mature filament. **(F)** Established NM2 filament associates with local monomers and nascent filaments, potentiating assembly. Sub-resolution NM2 filament stack/

cluster continues to grow. **(G–I)** Sub-resolution NM2 filament stack/cluster partitions. NM2 filaments bound to actin filaments moving apart in a parallel manner will remain in register to build a sarcomeric filament stack, while NM2 filaments bound to actin filaments moving apart in a disorganized manner will generate disordered filament clusters. **(J)** Separated, discrete myosin stacks and clusters continue to grow to build higher-order networks. **(K)** NM2 filaments disassemble, releasing monomers that are redistributed throughout the cell to feed RLC kinases (B) and elevate cytosolic monomer levels (C).

is consistent with recent EM data suggesting that 10S dimers and tetramers are the primary units of filament formation (Liu et al., 2017, 2020). In addition to localized actin rearrangements, tail retraction and pharmacological disruption of the actomyosin cytoskeleton (e.g., ROCK1/2 inhibition) could spur additional NM2 filament assembly through the release of NM2 monomer from previously assembled filaments. This sudden influx of NM2 monomers globally elevates the monomer concentration across the cell, facilitating nascent assembly by increasing the likelihood of NM2 monomer interactions. In each case, the dynamics of the actin network serve to modulate NM2 concentrations that drive the assembly of NM2 filaments.

Our model also implies an increased role for myosin:myosin interactions. In this regard, monomer:monomer, monomer:filament, and filament:filament interactions should be considered. It is known that multiple tail interactions between several monomers within an NM2 filament help to stabilize the structure (Ricketson et al., 2010). While the tail interactions surely dominate, numerous other interactions have been identified within the myosin holoenzyme (head–head, head–tail, light chain–tail, etc.) (Yang et al., 2020). It is quite possible that these low-affinity interactions also occur between NM2 monomers and filaments to contribute to the local enrichment of myosin. Additionally, NM2 filament stacks and clusters, concatenation, and partitioning have all been reported through a combination of in vitro and cellular studies (Beach et al., 2017; Fenix et al., 2016; Melli et al., 2018). This indicates myosin:myosin interactions beyond those occurring between monomer tails within a filament could be relevant, especially in subcellular regions with increased local monomer concentration. FRAP studies demonstrate that NM2 filament exchange kinetics are relatively rapid, with half-times of recovery typically reported as 10 s (Hu et al., 2017; Shutova et al., 2017). We hypothesize that once a nascent NM2 filament is established, transient interactions and rapid exchange kinetics enrich the local monomer concentration to increase the probability of additional filament assembly events (Israelachvili, 2011). We speculate this effective diffusion trap is the basis for the myosin-facilitated assembly that we observe in our data. Importantly, this model is not mutually exclusive with the potential for a nascent NM2 filament to enhance filament assembly via mechanosensitive feed-forward systems that alter local actin to favor assembly or initiate signaling events that lead to canonical myosin activation via RLC phosphorylation (Cavanaugh et al., 2020; Priya et al., 2015, 2016; Stephenson et al., 2019). Numerous mechanisms could be, and likely are, contributing: the nascent filament itself could serve as a scaffold to recruit binding partners, such as Rho GEFs (Jiao et al., 2018), to drive feed-forward signaling, or the nascent NM2 filament could pull on local actin to alter its tension state and increase affinity and dwell times for additional NM2 monomers/filaments (Luo et al., 2012; Uyeda et al., 2011) or for increased recruitment of upstream signaling components. Indeed, our observation of active RhoA flanking established myosin clusters is supportive of parallel mechanisms to amplify myosin filaments.

In conclusion, we propose that these concerted mechanisms collectively contribute to the rapid assembly and amplification of NM2 filaments to efficiently produce physiological levels of contraction in polarized migration. While it is most straightforward to experimentally observe these myosin dynamics in the lamellar regions of migrating cells, we believe this to be a universal mechanism of rapidly building contractility. Two additional areas of biology that have clear evidence for, and use of, rapid myosin filament assembly and amplification are the contractile ring (Henson et al., 2017) and adherens junction maturation (Yu-Kemp et al., 2022). In both contexts, higher-order myosin networks are observed and must develop rapidly to achieve the requisite contractility. The mechanisms that we outline here could help to drive the NM2 filament amplification in these dense areas. While additional work will be needed to confirm these mechanisms at work in dense regions, it is clear that in addition to biochemical regulation, myosin filament assembly and amplification are sensitive to biophysical constraints.

Materials and methods

Cell culture and transfection

Primary MEFs previously isolated (Beach et al., 2017) from EGFP NM2A knock-in mice (Zhang et al., 2012) were used within 10 passages. The immortalized fibroblast cell line, termed “JR20” cells (Rotty et al., 2015), was cultured within 15 passages. HEK293T cells were cultured to prepare lentivirus. Cells were cultured in Dulbecco’s modified Eagle’s Medium (#10-013-CV; Corning) supplemented with 10% FBEssence (#10803-034; Avantor Seradigm) and 1× antibiotic-antimycotic (#30-004-CI; Corning) at 37°C in 5% CO_2. All cells were grown on uncoated plastic tissue culture dishes and plated on #1.5 coverslips (#C8-1.5H-N; Cellvis) precoated overnight at 4°C with 10 µg/ml fibronectin (#FC01010MG; Thermo Fisher Scientific) and then rinsed with PBS before plating. Live-imaging experiments were conducted with Leibovit’s L-15 medium without phenol red (#21083027; Gibco) supplemented with 10% FBEssence.

Cells were transfected for CRISPR knock-in, lentivirus preparation, and the calcium and rho biosensor experiments using the LipoD293 (#SL100668; SignaGen) system. For CRISPR transfections, 1 million cells were transfected with 5 µg each of target and donor plasmid with the LipoD293 “Hard to Transfect” protocol. For lentivirus preparation, adherent HEK cells were transfected. Cells were transfected for molecular counting experiments using the Neon Electroporation system (Thermo Fischer Scientific) with 2 × 20 ms pulses of 1350V and 5 µg plasmid DNA into 400 k cells in a 100 µl reaction. For calcium activity experiments, cells were transfected with GCaMP7s

(Plasmid #104463; Addgene) (Dana et al., 2019) plated 24–48 h after transfection and 12–24 h before imaging, and then cells of average brightness were imaged. For RhoA activity experiments, cells were transfected with GFP-RhoA-AHPH (AKA "GFP-Rho-Bio") (Plasmid #68026; Addgene) (Piekny and Glotzer, 2008) with the same approach as described for the calcium experiments. Cells transfected with the protein nanocages for the molecular counting experiments were transfected with mem-EGFP-60mer or mem-EGFP-120mer, plated 48 h after transfection and 18–24 h before imaging. Cells transfected with EGFP-Actin (plasmid #31502; Addgene) (Watanabe and Mitchison, 2002) for the molecular counting experiments were transfected 4–6 h prior to imaging and plated immediately to achieve extremely low expression for single molecule identification. Primary MEFs used for long-term cell migration and JLY experiments were infected with viral media from HEK cells transfected with 3x-mScarlet-FTractin (Plasmid #112960; Addgene) (Chertkova et al., 2017, *Preprint*). Once stably expressing the 3x-mScarlet-FTractin, the cell line was restored and used within 10 passages. For the optogenetics experiments, a stable cell line was created using pLV-Stargazin-mTurquoise2-iLID (Plasmid #161001; Addgene) (Natwick and Collins, 2021) lentivirus and then transiently transfected with SspB-mApple-NM2A using LipoD293 transfection system. Cells were plated 24–48 h after transfection and 12–24 h before imaging. For all experiments using the Halo-tagged myosin line, cells were preincubated overnight with 0.1–1.0 nM Janelia Fluor-554 or -650 (JFX 554 and JFX 650) dye (Grimm et al., 2021).

Inhibitors were used at the following concentrations: Y27631 (#68801; EMD Millipore), 10 μM; LatrunculinB (#428020; EMD Millipore), 1.25 μM; Jasplakinolide (#420127; EMD Millipore), 2 μM. Drug treatments were prepared at a 2× solution in L-15 imaging media and then added to the wells at a 1:1 dilution while imaging. All cell lines were tested for mycoplasma once a month.

Generation of CRISPR knock-in cell lines

Halo-NM2A and mScarlet-NM2A knock-in cells were derived from JR20 parental fibroblasts using CRISPR/Cas9. We generated pSpCas9(BB)-2A-Puro (PX459) V2.0 (Plasmid #62988; Addgene) with target sequence 5′-AAACTTCATCAATAACCC GC-3′ using established protocols (Ran et al., 2013). To generate donor plasmids, pUC57 was digested with EcoR1 and Stu1 and purified. A four-piece Gibson assembly was then performed with three gBlocks (IDT): (1) a 794 bp 5′ HDR of genomic sequence immediate upstream of the endogenous start codon, (2) mScarlet fluorophore or HaloTag with an 18 amino acid GS-rich linker, (3) an 802 bp 3′ HDR of genomic sequence immediately downstream of the endogenous start codon with silent PAM site mutation. Fibroblasts were transfected with donor and target-Cas9 plasmids, single-cell sorted at 5–10 days after transfection. Individual clones were evaluated for knock-in via Western blotting and microscopy. Clones used in this study include Halo-NM2A clone 2 (H2A2) and mScarlet-NM2A clone 3 (S2A3).

Molecular cloning

To engineer photorecruitable NM2A, we introduced an SspB upstream of mApple in pmApple-NM2A. After digesting pmApple-NM2A with Age1, an SspB PCR product with flanking HDR arms was introduced via Gibson cloning in frame with mApple-NM2A.

Lentiviral stable cell lines

HEK293T cells were transfected using LipoD293 (#SL100668; Signagen) and the accompanying lentivirus generation transfection protocol. Briefly, cells were plated in a 6-cm dish and grown to 80–90% confluence. Approximately 1 h before transfection, media was changed on the cells. Transfection complex was created with LipoD293, packaging plasmic psPax (Plasmid #12260; Addgene), envelope plasmid PmD2.G (Plasmid #12259; Addgene), and lentiviral construct, and added dropwise to the dish. Media was changed at 24 h after transfection and collected at 48 and 72 h. Viral media was spun down at 1,000 *g* for 5 min and then filtered with a 0.45 μm filter. A 50% confluent 6 cm of cells were then infected with 48 h viral media. Viral media was removed after 24 h and cells were stored for future use after 3–5 days.

psPAX2 was a gift from Didier Trono (EPFL, Lausanne, Switzerland; plasmid #12260; Addgene; https://n2t.net/addgene:12260; RRID:Addgene 12260). pMD2.G was a gift from Didier Trono (plasmid #12259; Addgene; https://n2t.net/addgene:12259; RRID:Addgene 12259).

Light microscopy

Calcium, Rho, and Migration

Calcium and Rho imaging was performed on a Zeiss LSM 880 Airyscan with a 63× 1.4 NA objective in the "Airyscan Fast" acquisition mode. Time-lapse images of NM2 and calcium or rho biosensors were conducted at a 2.5 s or 10 s frame interval, respectively. Long-term migration imaging was performed on a Yokogawa W1 confocal spinning disk from 3i with a 40× 1.3 NA objective. Time-lapse images of NM2 (488) and actin (561) at 30% laser and 50 ms exposure per channel between 12 and 15 positions were acquired every minute for 8 h. Zeiss definite focus.2 was used to focus between timepoints and positions.

JL and JLY

JLY experiments were performed on a 3i confocal spinning disk with a 63× 1.4 NA objective. Time-lapse images of NM2 (488) and actin (561) at 30% laser and 50 ms exposure per channel. Four positions were acquired every 5 s for 10 min. Zeiss definite focus.2 was used to focus between timepoints and positions. After 5 min, drug cocktails prepared at a 2× concentration were added 1:1 with the media in the well while imaging to ensure rapid treatment. Cells were imaged until they ripped apart from the drug treatment and then an equal number of frames before and after treatment were used for analysis.

iLID photo-recruitment

Optogenetic imaging was performed on a Zeiss LSM 880 Airyscan with a 63× 1.4 NA objective in the "Airyscan Fast" acquisition mode at 30°C. Due to low levels of leaking laser light at the center of the field of view that could stimulate the LOV2 in the iLID system when using "Bleaching" settings required for spatial stimulation, we collected sequential time-lapses at 10-s intervals with 0.85 μs pixel dwell, 2× frame averaging. With the lamellar protrusion in the middle of the field of view, we first collected 15 frames prestimulation (without “Bleaching” engaged) for baseline intensity measurements. Then, we collected a second time-lapse with “Bleaching” engaged with a 50-pixel (3.67 μm) ROI at the center of the field of view (x,y = 0,0 in Zen Black) for 15 min. Bleaching settings in the ROI were 50 iterations, 4.54 μs pixel dwell, and 488 laser at 0.30% power. These two time lapses were concatenated in FIJI for subsequent analyses (see below).

Molecular counting

For all molecular counting experiments, standard candle controls and EGFP-NM2A imaging were performed each day within 6 h of each other using identical laser and acquisition settings (see “Cell culture and Transfections” for additional details). Live molecular counting experiments were performed on a Zeiss LSM 880 Airyscan with a 63× 1.4 NA objective in the “Airyscan Fast” acquisition mode. Argon laser at 0.9% power with 0.83 μs pixel dwell, a 4× frame averaging was used for all images acquired for the standard curve and live imaging of NM2 to be counted. Time-lapse images of NM2 were conducted with identical laser power, pixel dwell, and averaging at a 5 s frame interval.

Fixed molecular counting experiments were performed on a Zeiss LSM 880 Airyscan with a 100× 1.4 NA objective in the “Airyscan Fast” acquisition mode. Argon laser at 9% power with 0.98 μs pixel dwell, a 4× frame averaging was used for all images acquired for the standard curve and live imaging of NM2 to be counted. Time-lapse images of NM2 were conducted with identical laser power, pixel dwell, and averaging at a 5-s frame interval.

Correlative light and electron microscopy

Round 25-mm coverslips were squeaky-cleaned (Waterman-Storer, 2001) and plasma-cleaned before coating with 20 μg/ml Human Plasma Fibronectin (#FC010; EMD Millipore) at 37°C for 1 h. After fibronectin coating and subsequent PBS washes, PDMS strips ~5 mm in width and 25 mm in length, were placed to bisect the circular coverslip. Cells were plated at 75% confluence and incubated overnight. 20–24 h after plating, PDMS strips were removed and the media changed twice to remove any lifted cells. Cell unroofing was performed 12–18 h after PDMS strip removal as described previously (Sochacki et al., 2017; Sochacki and Taraska, 2017). Briefly, coverslips were individually taped onto a 6-cm petri dish and covered with PBS. Then, they were rinsed with intracellular buffer (70 mM KCL, 30 mM HEPES maintained at pH 7.4 with KOH, 5 mM $MgCL_2$, 3 mM EGTA) and then cell edges were “glued” down with a 30 s treatment of 0.08% Poly-*L*-Lysine in intracellular buffer. Then cells were manually unroofed by spraying 1 ml of 3% paraformaldehyde (#15710; Electron Microscopy Sciences) and 1% glutaraldehyde (#16216; Electron Microscopy Sciences) in intracellular buffer through a 25 gauge needle along the line of the PDMS “wound” from a distance of 1 cm. Fresh fixative was added to fully submerge the coverslips to fix for 30 min at room temperature. Coverslips were then rinsed with PBS and then removed from petri dishes to incubate in 1:50 phalloidin-555 (#A34055; Thermo Fisher Scientific) face down on parafilm for 30 min at RT. Immediately after phalloidin staining, coverslips were carefully flipped over, avoiding any sliding, and placed in a PBS wash. The coverslips were then mounted in a magnetic chamber in PBS and immediately imaged on the Zeiss LSM 880 Airyscan. Cells that appeared unroofed based on phalloidin intensity were selected within a 1 mm diameter and the coverslip was marked for that region with a diamond tip objective. Within the marked region, NM2 and actin were imaged at 63× 1.4 NA oil in “SR” mode and then 40× 1.3 NA oil tilescan in “Fast” mode. Coverslips were then imaged using an EVOS phase contrast microscope at 20×, 10×, and 4×. Images were then organized to create a map back to the same imaged ROI after platinum replica preparation. After fluorescence imaging, coverslips were placed in fixative and flipped over onto a glass slide. The coverslips were immobilized with epoxy resin, sealed with VALAP, and shipped overnight at 4°C to the Taraska lab at NIH for the PREM workflow.

Platinum replica sample preparation was performed as described in Sochacki et al. (2017); Sochacki and Taraska (2017). Briefly, coverslips were placed in 0.1% tannic acid for 20 min, rinsed 4× in water, 0.1% uranyl acetate for 20 min, rinsed 2× in water, and then dehydrated gradually with increasing concentrations of ethanol (15, 30, 50, 70, 80, 90% up to being rinsed 3× in 100% ethanol) prior to critical point drying (895; Tousimis). After critical point drying, the coverslips were trimmed down with a diamond scriber. Samples were rotary coated with a 2–3 nm coat of platinum-carbon at a 17° angle, then 5–6 nm carbon at a 90° angle (9010; RMC). The coverslips were imaged with 20× phase contrast light microscopy to find the cells that were previously mapped during fluorescence imaging. The coverslip was then placed face up on the air/water interface of 5% hydrofluoric acid until the coverslip dropped into the solution leaving the platinum replica sitting on the surface. The replica was rinsed with water and lifted with a 4-mm circular loop onto a formvar/carbon-coated 75-mesh copper grid (01802-F; Ted Pella). The grid was again imaged with 20× phase contrast light microscopy to confirm that the replica transfer went smoothly and to identify the area of interest on the grid. Transmission electron microscopy (TEM) was performed with montaging on a FEI Tecnai T12 equipped with a Gatan Rio-9 camera and SerialEM freeware (Mastronarde, 2005). Correlation of fluorescence and platinum replica electron micrographs was performed using Matlab correlation software (Sochacki et al., 2017). Major structures in the actin channel (e.g., large bundles or unique branching) were used to correlate images, with a minimum of 20 points used to correlate.

Image analysis

Filament appearances

Qualitative analysis of filament appearances in individual examples in figures (Fig. 1 A, Fig. 2 E, Fig. 3, A–C, and Fig. 5 G) was conducted in FIJI by making sum-time projections for every 10 frames. Kymographs (Fig. 1, B and C; and Fig. 2, B and D) were generated in FIJI using the KymoResliceWide plugin with a line width of 21 and a maximum intensity value across the width. Appearance correlations (Fig. 1 C and Fig. 2 C) were quantified from kymographs generated as described above for individual filament appearances and presented as a percentage of total appearances with standard deviation calculated between the four experimental days. Quantitative filament appearance comparisons (Fig. 1 D, Fig. 2 F, and Fig. 3 D) were produced by manually identifying the filament appearances in movies and then comparing the normalized appearance rates before and after drug administration (normalized to pretreatment frames). For the MLCK and ROCK inhibitors, 5 min pre-treatment and 10 min post-treatment were analyzed. For JL/JLY experiments, an equal number of pre- and post-treatment frames were analyzed—the length of which was cut off by cells ripping from the actin stalling treatment. For JL and JLY cells, between 2 and 5 min of data were used for these quantification windows, depending on the cell ripping, and 5 min pre- and post-treatment was used for the DMSO control cells.

iLID photo-recruitment

Analysis was performed in FIJI. Three regions were analyzed for each cell. The "activation" ROI was defined as a 50-pixel-wide circular ROI identical to the region of blue light exposure. The "retrograde" ROI was defined as a 100-pixel-wide and 50-pixel-long rectangular ROI (with the overlapping half-circle included in the activation ROI removed; see cartoon in Fig. 4) behind the activation ROI in the direction of retrograde flow. A "control" ROI was manually determined for each cell. For this, we included the largest lamellar region present within the boundary of the cell edge throughout the experiment and excluded regions in which denser transverse arcs encroached. For each region, the background-subtracted mean intensity was normalized to the mean of the 15 frames prior to photorecruitment.

Molecular counting

Image analysis was performed using custom-written Python analysis software (https://github.com/m-a-q or https://github.com/OakesLab). Images were sum-projected in Z, and then cell masks were generated for each image and each frame for time series. For candle images, single frames were analyzed and local peaks (or puncta) were identified within the cell mask. The intensity of a 14 by 14 pixel box around each peak was used to filter out any candles that were side by side. The intensity of the top of bottom z slices where the peaks are identified in X and Y was used to filter out candles that were not fully within the Z range that was acquired. Once unsuitable peaks were filtered out, the remaining list of peak positions was used to quantify the sum intensity of a 14 by 14 pixel box around the peak coordinates. Candle intensities were then plotted in histograms and then plotted by the number of GFPs present in the molecules. The intensity of a single GFP was found from linear regression analysis.

Images of NM2 were analyzed using trackpy (https://github.com/soft-matter/trackpy) (Crocker and Grier, 1996) to first identify NM2 filament clusters as they appear and flow back with retrograde flow. A 35 by 35 pixel box around the particle centroid was summed to quantify the fluorescent intensity, then divided by the intensity of a single GFP, and then divided by 2 to get the number of NM2 monomers present in the structure at any given frame. This was compared with the rate of track appearance from the same trackpy analysis. For partitioning analysis, individual tracks were then further tracked to identify local peaks within the growing cluster to count the number of NM2 head groups that could be resolved. Based on the number of resolvable head groups, we determined the partitioning state of the structure.

Statistical analysis

To compare the number of NM2 filament appearance rates (Fig. 1 D, Fig. 2 F, and Fig. 4 D), we used a non-parametric Wilcoxon matched-pairs signed rank test performed comparing "pre" and "post" frames for each cell. Statistical analysis was performed using Prism (GraphPad). P values <0.05 were considered significant.

Intensity histograms (Fig. 6.C) were fit to Gaussians, and linear regression analysis was used on the calibration curves (Fig. 6 D and Fig. 7 E) to determine the value of a single GFP. Statistical analysis was performed using the stats module from scipy.

Online supplemental material

Fig. S1 displays leading edge retractions with EGFP-VASP, in which nascent NM2A filaments appear following a leading edge retraction. Fig. S2 displays depictions and examples of our molecular counting workflow. Fig. S3 uses EM-guided bounding boxes of NM2 filaments to demonstrate that many filaments can fit within our light microscopy pixels and voxels. Video 1 demonstrates our filament appearance tracking proficiency. Video 2 displays EGFP-NM2A filament appearances following leading edge retractions. Videos 3, 4, and 5 display our ability to stall lamellar actin dynamics with JL treatment, and examples of NM2A filament appearance upon DMSO or JL treatment. Video 6 displays long-term time-lapse imaging of EGFP-NM2A fibroblasts, while Video 7 displays a shorter time window in which a tail retraction correlates with an increase in lamellar NM2 filament appearances. Videos 8 and 9 display NM2 appearances upon ROCKi (Y27) and JLY treatment, respectively. Video 10 displays iLID-based cortical recruitment of exogenous NM2A is sufficient to induce filament assembly and recruitment of endogenous NM2A. Video 11 displays an example of robust NM2 filament cluster growth in the lamella. Video 12 displays our characterization of 2-, 3-, and 4-puncta EGFP-NM2A structures in time-lapse imaging.

Data availability

The data that support the findings of this study are available upon reasonable request from the corresponding author (Jordan Beach).

Acknowledgments

We thank the rest of the Beach and Oakes laboratories at the Loyola University Chicago, Maywood, IL for many helpful discussions. We thank L.D. Lavis and J.B. Grimm (Howard Hughes Medical Institute, Janelia Research Campus, Ashburn, VA, USA) for the gift of JF and JFX dyes. We thank Haotian Lei and Yanxiang Cui for TEM microscope maintenance as part of the

NIDDK cryo-EM facility at the National Institutes of Health Bethesda campus.

Research reported in this publication was supported by the Maximizing Investigators' Research Award (MIRA R35) from the National Institute of General Medical Sciences (NIGMS) of the National Institutes of Health (NIH) #R35GM138183 to J.R. Beach, National Science Foundation CAREER Award #2000554 and NIH NIGMS (award #R01-GM148644) to P.W. Oakes, and the National Science Foundation Graduate Research Fellowship #DGE-1842190 to M.A. Quintanilla.

Author contributions: M.A. Quintanilla, P.W. Oakes, and J.R. Beach designed the research. M.A. Quintanilla, K.A. Sochacki, H. Wu, H. Patel, and J.R. Beach performed experiments. M.A. Quintanilla, S. Chandrasekar, P.W. Oakes, and J.R. Beach analyzed data. J.D. Rotty and J.E. Bear contributed critical cell lines. F. Korobova, J.W. Taraska, and M. Akamatsu contributed to experimental techniques. M.A. Quintanilla, P.W. Oakes, and J.R. Beach wrote the manuscript with critical feedback from co-authors.

Disclosures: The authors declare no competing interests exist.

Submitted: 5 May 2023
Revised: 2 January 2024
Accepted: 26 January 2024

References

Adelstein, R.S., and M.A. Conti. 1975. Phosphorylation of platelet myosin increases actin-activated myosin ATPase activity. *Nature*. 256:597–598. https://doi.org/10.1038/256597a0

Akamatsu, M., R. Vasan, D. Serwas, M. Ferrin, P. Rangamani and D.G. Drubin. 2019. Principles of self-organization and load adaptation by the actin cytoskeleton during clathrin-mediated endocytosis. *Elife*. 9:e49840. https://doi.org/10.7554/eLife.49840

Andrews, N.L., K.A. Lidke, J.R. Pfeiffer, A.R. Burns, B.S. Wilson, J.M. Oliver, and D.S. Lidke. 2008. Actin restricts FcepsilonRI diffusion and facilitates antigen-induced receptor immobilization. *Nat. Cell Biol.* 10: 955–963. https://doi.org/10.1038/ncb1755

Applegate, D., and J.D. Pardee. 1992. Actin-facilitated assembly of smooth muscle myosin induces formation of actomyosin fibrils. *J. Cell Biol.* 117: 1223–1230. https://doi.org/10.1083/jcb.117.6.1223

Beach, J.R., K.S. Bruun, L. Shao, D. Li, Z. Swider, K. Remmert, Y. Zhang, M.A. Conti, R.S. Adelstein, N.M. Rusan, et al. 2017. Actin dynamics and competition for myosin monomer govern the sequential amplification of myosin filaments. *Nat. Cell Biol.* 19:85–93. https://doi.org/10.1038/ncb3463

Beach, J.R., L. Shao, K. Remmert, D. Li, E. Betzig, and J.A. Hammer III. 2014. Nonmuscle myosin II isoforms coassemble in living cells. *Curr. Biol.* 24: 1160–1166. https://doi.org/10.1016/j.cub.2014.03.071

Bieling, P., T.-D. Li, J. Weichsel, R. McGorty, P. Jreij, B. Huang, D.A. Fletcher, and R.D. Mullins. 2016. Force feedback controls motor activity and mechanical properties of self-assembling branched actin networks. *Cell*. 164:115–127. https://doi.org/10.1016/j.cell.2015.11.057

Billington, N., A. Wang, J. Mao, R.S. Adelstein, and J.R. Sellers. 2013. Characterization of three full-length human nonmuscle myosin II paralogs. *J. Biol. Chem.* 288:33398–33410. https://doi.org/10.1074/jbc.M113.499848

Burnette, D.T., S. Manley, P. Sengupta, R. Sougrat, M.W. Davidson, B. Kachar, and J. Lippincott-Schwartz. 2011. A role for actin arcs in the leading-edge advance of migrating cells. *Nat. Cell Biol.* 13:371–381. https://doi.org/10.1038/ncb2205

Cavanaugh, K.E., M.F. Staddon, E. Munro, S. Banerjee, and M.L. Gardel. 2020. Rhoa mediates epithelial cell shape changes via mechanosensitive endocytosis. *Dev. Cell*. 52:152–166.e5. https://doi.org/10.1016/j.devcel.2019.12.002

Chertkova, A.O., M. Mastop, M. Postma, N.v. Bommel, S.d. Niet, K.L. Batenburg, L. Joosen, T.W.J. Gadella, Y. Okada, and J. Goedhart. 2017. Robust and bright genetically encoded fluorescent markers for highlighting structures and compartments in mammalian cells. *bioRxiv*. https://doi.org/10.1101/160374v2 (Preprint posted July 06, 2017).

Chou, W-H., M. Molaei, H. Wu, P.W. Oakes, J.R. Beach, and M.L. Gardel. 2024. Limiting pool and actin architecture controls myosin cluster sizes in adherent cells. *Biophys J*. 123:157–171. https://doi.org/10.1016/j.bpj.2023.12.004

Craig, R., R. Smith, and J. Kendrick-Jones. 1983. Light-chain phosphorylation controls the conformation of vertebrate non-muscle and smooth muscle myosin molecules. *Nature*. 302:436–439. https://doi.org/10.1038/302436a0

Crocker, J.C., and D.G. Grier. 1996. Methods of digital video microscopy for colloidal studies. *J. Colloid Interf. Sci.* 179. 298–310. https://doi.org/10.1006/jcis.1996.0217

Dana, H., Y. Sun, B. Mohar, B.K. Hulse, A.M. Kerlin, J.P. Hasseman, G. Tsegaye, A. Tsang, A. Wong, R. Patel, et al. 2019. High-performance calcium sensors for imaging activity in neuronal populations and microcompartments. *Nat. Methods*. 16:649–657. https://doi.org/10.1038/s41592-019-0435-6

Fenix, A.M., A.M. Taneja, C.A. Buttler, J. Lewis, S.B. Van Engelenburg, R. Ohi, and D.T. Burnette. 2016. Expansion and concatenation of non-muscle myosin IIA filaments drive cellular contractile system formation during interphase and mitosis. *Mol. Biol. Cell*. 27:1465–1478. https://doi.org/10.1091/mbc.E15-10-0725

Gauthier, N.C., T.A. Masters, and M.P. Sheetz. 2012. Mechanical feedback between membrane tension and dynamics. *Trends Cell Biol.* 22:527–535. https://doi.org/10.1016/j.tcb.2012.07.005

Greene, L.E., and J.R. Sellers. 1987. Effect of phosphorylation on the binding of smooth muscle heavy meromyosin X ADP to actin. *J. Biol. Chem.* 262: 4177–4181. https://doi.org/10.1016/S0021-9258(18)61329-8

Grewe, J. and U.S. Schwarz. 2020. Mechanosensitive self-assembly of myosin II minifilaments. *Physi. Rev. E*. 101. 022402. https://doi.org/10.1103/PhysRevE.101.022402

Grimm, J.B., L. Xie, J.C. Casler, R. Patel, A.N. Tkachuk, N. Falco, H. Choi, J. Lippincott-Schwartz, T.A. Brown, B.S. Glick, et al. 2021. A general method to improve fluorophores using deuterated auxochromes. *JACS Au*. 1:690–696. https://doi.org/10.1021/jacsau.1c00006

Guntas, G., R.A. Hallett, S.P. Zimmerman, T. Williams, H. Yumerefendi, J.E. Bear, and B. Kuhlman. 2015. Engineering an improved light-induced dimer (iLID) for controlling the localization and activity of signaling proteins. *Proc. Natl. Acad. Sci. USA*. 112:112–117. https://doi.org/10.1073/pnas.1417910112

Henson, J.H., C.E. Ditzler, A. Germain, P.M. Irwin, E.T. Vogt, S. Yang, X. Wu, and C.B. Shuster. 2017. The ultrastructural organization of actin and myosin II filaments in the contractile ring: New support for an old model of cytokinesis. *Mol. Biol. Cell*. 28:613–623. https://doi.org/10.1091/mbc.e16-06-0466

Hirakawa, R., Y. Nishikawa, T.Q.P. Uyeda, and K. Tokuraku. 2017. Unidirectional growth of heavy meromyosin clusters along actin filaments revealed by real-time fluorescence microscopy. *Cytoskeleton*. 74: 482–489. https://doi.org/10.1002/cm.21408

Hsia, Y., J.B. Bale, S. Gonen, D. Shi, W. Sheffler, K.K. Fong, U. Nattermann, C. Xu, P.-S. Huang, R. Ravichandran, et al. 2016. Design of a hyperstable 60-subunit protein dodecahedron. [corrected]. *Nature*. 535:136–139. https://doi.org/10.1038/nature18010

Hu, S., K. Dasbiswas, Z. Guo, Y.-H. Tee, V. Thiagarajan, P. Hersen, T.-L. Chew, S.A. Safran, R. Zaidel-Bar, and A.D. Bershadsky. 2017. Long-range self-organization of cytoskeletal myosin II filament stacks. *Nat. Cell Biol.* 19: 133–141. https://doi.org/10.1038/ncb3466

Ikebe, M., and D.J. Hartshorne. 1986. Proteolysis and actin-binding properties of 10S and 6S smooth muscle myosin: Identification of a site protected from proteolysis in the 10S conformation and by the binding of actin. *Biochemistry*. 25:6177–6185. https://doi.org/10.1021/bi00368a052

Israelachvili, J.N. 2011. 19: Thermodynamic principles of self-assembly. In Intermolecular and Surface Forces. Third edition. J.N. Israelachvili, editor. Academic Press, San Diego. 503–534. https://doi.org/10.1016/B978-0-12-391927-4.10019-2

Ji, L., J. Lim, and G. Danuser. 2008. Fluctuations of intracellular forces during cell protrusion. *Nat. Cell Biol.* 10:1393–1400. https://doi.org/10.1038/ncb1797

Jiao, M., D. Wu, and Q. Wei. 2018. Myosin II-interacting guanine nucleotide exchange factor (MYOGEF) promotes bleb retraction via stimulating cortex reassembly at the bleb membrane. *Mol. Biol. Cell* 29:643–656. https://doi.org/10.1091/mbc.E17-10-0579

Johnson, H.W., and M.J. Schell. 2009. Neuronal IP3 3-kinase is an F-actin-bundling protein: Role in dendritic targeting and regulation of spine morphology. *Mol. Biol. Cell*. 20:5166–5180. https://doi.org/10.1091/mbc.e09-01-0083

Kendrick-Jones, J., R.C. Smith, R. Craig, and S. Citi. 1987. Polymerization of vertebrate non-muscle and smooth muscle myosins. *J. Mol. Biol.* 198: 241–252. https://doi.org/10.1016/0022-2836(87)90310-X

Laevsky, G., and D.A. Knecht. 2003. Cross-linking of actin filaments by myosin II is a major contributor to cortical integrity and cell motility in restrictive environments. *J. Cell Sci.* 116:3761–3770. https://doi.org/10.1242/jcs.00684

Liu, X., N. Billington, S. Shu, S.-H. Yu, G. Piszczek, J.R. Sellers, and E.D. Korn. 2017. Effect of ATP and regulatory light-chain phosphorylation on the polymerization of mammalian nonmuscle myosin II. *Proc. Natl. Acad. Sci. USA*. 114:E6516–E6525. https://doi.org/10.1073/pnas.1702375114

Liu, X., S. Shu, and E.D. Korn. 2020. Muscle myosins form folded monomers, dimers, and tetramers during filament polymerization in vitro. *Proc. Natl. Acad. Sci. USA*. 117:15666–15672. https://doi.org/10.1073/pnas.2001892117

Luo, T., K. Mohan, V. Srivastava, Y. Ren, P.A. Iglesias, and D.N. Robinson. 2012. Understanding the cooperative interaction between myosin II and actin cross-linkers mediated by actin filaments during mechanosensation. *Biophys. J.* 102:238–247. https://doi.org/10.1016/j.bpj.2011.12.020

Mahajan, R.K., and J.D. Pardee. 1996. Assembly mechanism of Dictyostelium myosin II: Regulation by K^+, Mg^{2+}, and actin filaments. *Biochemistry*. 35: 15504–15514. https://doi.org/10.1021/bi9618981

Mastronarde, D.N. 2005. Automated electron microscope tomography using robust prediction of specimen movements. *J. Struct. Biol.* 152:36–51. https://doi.org/10.1016/j.jsb.2005.07.007

Melli, L., N. Billington, S.A. Sun, J.E. Bird, A. Nagy, T.B. Friedman, Y. Takagi, and J.R. Sellers. 2018. Bipolar filaments of human nonmuscle myosin 2-A and 2-B have distinct motile and mechanical properties. *Elife*. 7: e32871. https://doi.org/10.7554/eLife.32871

Millius, A., N. Watanabe, and O.D. Weiner. 2012. Diffusion, capture and recycling of SCAR/WAVE and Arp2/3 complexes observed in cells by single- molecule imaging. *J. Cell Sci.* 125. 1165–1176. https://doi.org/10.1242/jcs.091157

Natwick, D.E., and S.R. Collins. 2021. Optimized iLID membrane anchors for local optogenetic protein recruitment. *ACS Synth. Biol.* 10:1009–1023. https://doi.org/10.1021/acssynbio.0c00511

Nickaeen, M., I.L. Novak, S. Pulford, A. Rumack, J. Brandon, B.M. Slepchenko, and A. Mogilner. 2017. A free-boundary model of a motile cell explains turning behavior. *PLoS Comput. Biol.* 13:e1005862. https://doi.org/10.1371/journal.pcbi.1005862

Niederman, R., and T.D. Pollard. 1975. Human platelet myosin. II. in vitro assembly and structure of myosin filaments. *J. Cell Biol.* 67:72–92. https://doi.org/10.1083/jcb.67.1.72

Peng, G.E., S.R. Wilson, and O.D. Weiner. 2011. A pharmacological cocktail for arresting actin dynamics in living cells. *Mol. Biol. Cell*. 22:3986–3994. https://doi.org/10.1091/mbc.E11-04-0379

Piekny, A.J., and M. Glotzer. 2008. Anillin is a scaffold protein that links RhoA, actin, and myosin during cytokinesis. *Curr. Biol.* 18:30–36. https://doi.org/10.1016/j.cub.2007.11.068

Priya, R., G.A. Gomez, S. Budnar, S. Verma, H.L. Cox, N.A. Hamilton, and A.S. Yap. 2015. Feedback regulation through myosin II confers robustness on RhoA signalling at E-cadherin junctions. *Nat. Cell Biol.* 17:1282–1293. https://doi.org/10.1038/ncb3239

Priya, R., K. Wee, S. Budnar, G.A. Gomez, A.S. Yap, and M. Michael. 2016. Coronin 1B supports RhoA signaling at cell-cell junctions through Myosin II. *Cell Cycle*. 15:3033–3041. https://doi.org/10.1080/15384101.2016.1234549

Quintanilla, M.A., J.A. Hammer, and J.R. Beach. 2023. Non-muscle myosin 2 at a glance. *J. Cell Sci.* 136:jcs260890. https://doi.org/10.1242/jcs.260890

Ran, F.A., P.D. Hsu, J. Wright, V. Agarwala, D.A. Scott, and F. Zhang. 2013. Genome engineering using the CRISPR-Cas9 system. *Nat. Protoc.* 8: 2281–2308. https://doi.org/10.1038/nprot.2013.143

Ricketson, D., C.A. Johnston, and K.E. Prehoda. 2010. Multiple tail domain interactions stabilize nonmuscle myosin II bipolar filaments. *Proc. Natl. Acad. Sci. USA*. 107:20964–20969. https://doi.org/10.1073/pnas.1007025107

Robin, F.B., W.M. McFadden, B. Yao, and E.M. Munro. 2014. Single-molecule analysis of cell surface dynamics in *Caenorhabditis elegans* embryos. *Nat. Methods*. 11:677–682. https://doi.org/10.1038/nmeth.2928

Rotty, J.D., C. Wu, E.M. Haynes, C. Suarez, J.D. Winkelman, H.E. Johnson, J.M. Haugh, D.R. Kovar, and J.E. Bear. 2015. Profilin-1 serves as a gatekeeper for actin assembly by Arp2/3-dependent and -independent pathways. *Dev. Cell*. 32:54–67. https://doi.org/10.1016/j.devcel.2014.10.026

Sellers, J.R. 1985. Mechanism of the phosphorylation-dependent regulation of smooth muscle heavy meromyosin. *J. Biol. Chem.* 260:15815–15819. https://doi.org/10.1016/S0021-9258(17)36331-7

Shutova, M.S., S.B. Asokan, S. Talwar, R.K. Assoian, J.E. Bear, and T.M. Svitkina. 2017. Self-sorting of nonmuscle myosins IIA and IIB polarizes the cytoskeleton and modulates cell motility. *J. Cell Biol.* 216:2877–2889. https://doi.org/10.1083/jcb.201705167

Shutova, M.S., W.A. Spessott, C.G. Giraudo, and T. Svitkina. 2014. Endogenous species of mammalian nonmuscle myosin IIA and IIB include activated monomers and heteropolymers. *Curr. Biol.* 24:1958–1968. https://doi.org/10.1016/j.cub.2014.07.070

Sochacki, K.A., A.M. Dickey, M.-P. Strub, and J.W. Taraska. 2017. Endocytic proteins are partitioned at the edge of the clathrin lattice in mammalian cells. *Nat. Cell Biol.* 19:352–361. https://doi.org/10.1038/ncb3498

Sochacki, K.A., B.L. Heine, G.J. Haber, J.R. Jimah, B. Prasai, M.A. Alfonzo-Méndez, A.D. Roberts, A. Somasundaram, J.E. Hinshaw, and J.W. Taraska. 2021. The structure and spontaneous curvature of clathrin lattices at the plasma membrane. *Dev. Cell*. 56:1131–1146.e3. https://doi.org/10.1016/j.devcel.2021.03.017

Sochacki, K.A., and J.W. Taraska. 2017. Correlative fluorescence super-resolution localization microscopy and platinum replica EM on unroofed cells. *Methods Mol. Biol.* 1663:219–230. https://doi.org/10.1007/978-1-4939-7265-4_18

Stephenson, R.E., T. Higashi, I.S. Erofeev, T.R. Arnold, M. Leda, A.B. Goryachev, and A.L. Miller. 2019. Rho flares repair local tight junction leaks. *Dev. Cell*. 48:445–459.e5. https://doi.org/10.1016/j.devcel.2019.01.016

Svitkina, T. 2022. Imaging cytoskeleton components by electron microscopy. *Methods Mol. Biol.* 2364:25–52. https://doi.org/10.1007/978-1-0716-1661-1_2

Svitkina, T.M., and G.G. Borisy. 1998. Correlative light and electron microscopy of the cytoskeleton of cultured cells. *Methods Enzymol.* 298: 570–592. https://doi.org/10.1016/S0076-6879(98)98045-4

Svitkina, T.M., I.G. Surguchova, A.B. Verkhovsky, V.I. Gelfand, M. Moeremans, and J. De Mey. 1989. Direct visualization of bipolar myosin filaments in stress fibers of cultured fibroblasts. *Cell Motil. Cytoskeleton*. 12: 150–156. https://doi.org/10.1002/cm.970120304

Totsukawa, G., Y. Yamakita, S. Yamashiro, D.J. Hartshorne, Y. Sasaki, and F. Matsumura. 2000. Distinct roles of ROCK (Rho-kinase) and MLCK in spatial regulation of MLC phosphorylation for assembly of stress fibers and focal adhesions in 3T3 fibroblasts. *J. Cell Biol.* 150:797–806. https://doi.org/10.1083/jcb.150.4.797

Uyeda, T.Q.P., Y. Iwadate, N. Umeki, A. Nagasaki, and S. Yumura. 2011. Stretching actin filaments within cells enhances their affinity for the myosin II motor domain. *PLoS One*. 6:e26200. https://doi.org/10.1371/journal.pone.0026200

Verkhovsky, A.B., I.G. Surgucheva, T.M. Svitkina, I.S. Tint, and V.I. Gelfand. 1987. Organization of stress fibers in cultured fibroblasts after extraction of actin with bovine brain gelsolin-like protein. *Exp. Cell Res.* 173: 244–255. https://doi.org/10.1016/0014-4827(87)90349-1

Verkhovsky, A.B., T.M. Svitkina, and G.G. Borisy. 1995. Myosin II filament assemblies in the active lamella of fibroblasts: Their morphogenesis and role in the formation of actin filament bundles. *J. Cell Biol.* 131:989–1002. https://doi.org/10.1083/jcb.131.4.989

Watanabe, N., and T.J. Mitchison. 2002. Single-molecule speckle analysis of actin filament turnover in lamellipodia. *Science*. 295:1083–1086. https://doi.org/10.1126/science.1067470

Waterman-Storer, C.M. 2001. Microtubule/organelle motility assays. *Curr. Protoc. Cell Biol.* 13:Unit 13.1. https://doi.org/10.1126/science.1067470

Yang, S., P. Tiwari, K.H. Lee, O. Sato, M. Ikebe, R. Padrón, and R. Craig. 2020. Cryo-EM structure of the inhibited (10s) form of myosin II. *Nature*. 588: 521–525. https://doi.org/10.1038/s41586-020-3007-0

Yi, J., X.S. Wu, T. Crites, and J.A. Hammer III. 2012. Actin retrograde flow and actomyosin II arc contraction drive receptor cluster dynamics at the immunological synapse in Jurkat T cells. *Mol. Biol. Cell*. 23:834–852. https://doi.org/10.1091/mbc.e11-08-0731

Yu-Kemp, H.-C., R.A. Szymanski, D.B. Cortes, N.C. Gadda, M.L. Lillich, A.S. Maddox, and M. Peifer. 2022. Micron-scale supramolecular myosin arrays help mediate cytoskeletal assembly at mature adherens junctions. *J. Cell Biol.* 221:e202103074. https://doi.org/10.1083/jcb.202103074

Zhang, Y., M.A. Conti, D. Malide, F. Dong, A. Wang, Y.A. Shmist, C. Liu, P. Zerfas, M.P. Daniels, C.-C. Chan, et al. 2012. Mouse models of MYH9-related disease: Mutations in nonmuscle myosin II-A. *Blood*. 119: 238–250. https://doi.org/10.1182/blood-2011-06-358853

Supplemental material

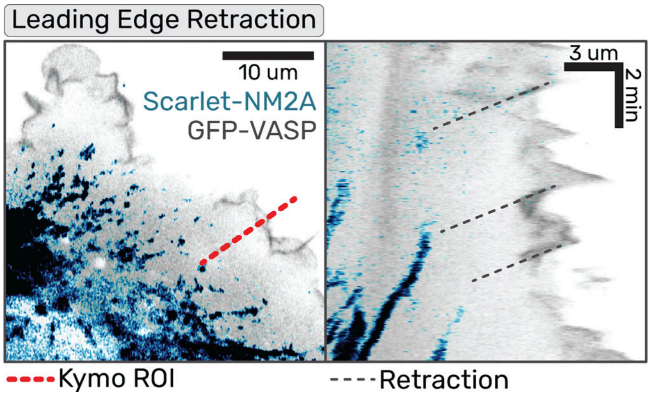

Figure S1. **Leading edge retractions with EGFP-VASP.** Scarlet-NM2A cells transiently expressing mEGFP-VASP imaged with confocal microscopy every second. The image is a sum intensity projection of a z-stack with NM2 in blue and VASP in inverted grayscale. Scale bar = 10 µm. The red line indicates the ROI used for subsequent kymograph in the right panel. Gray dotted lines connect leading edge retractions with NM2 filament appearance.

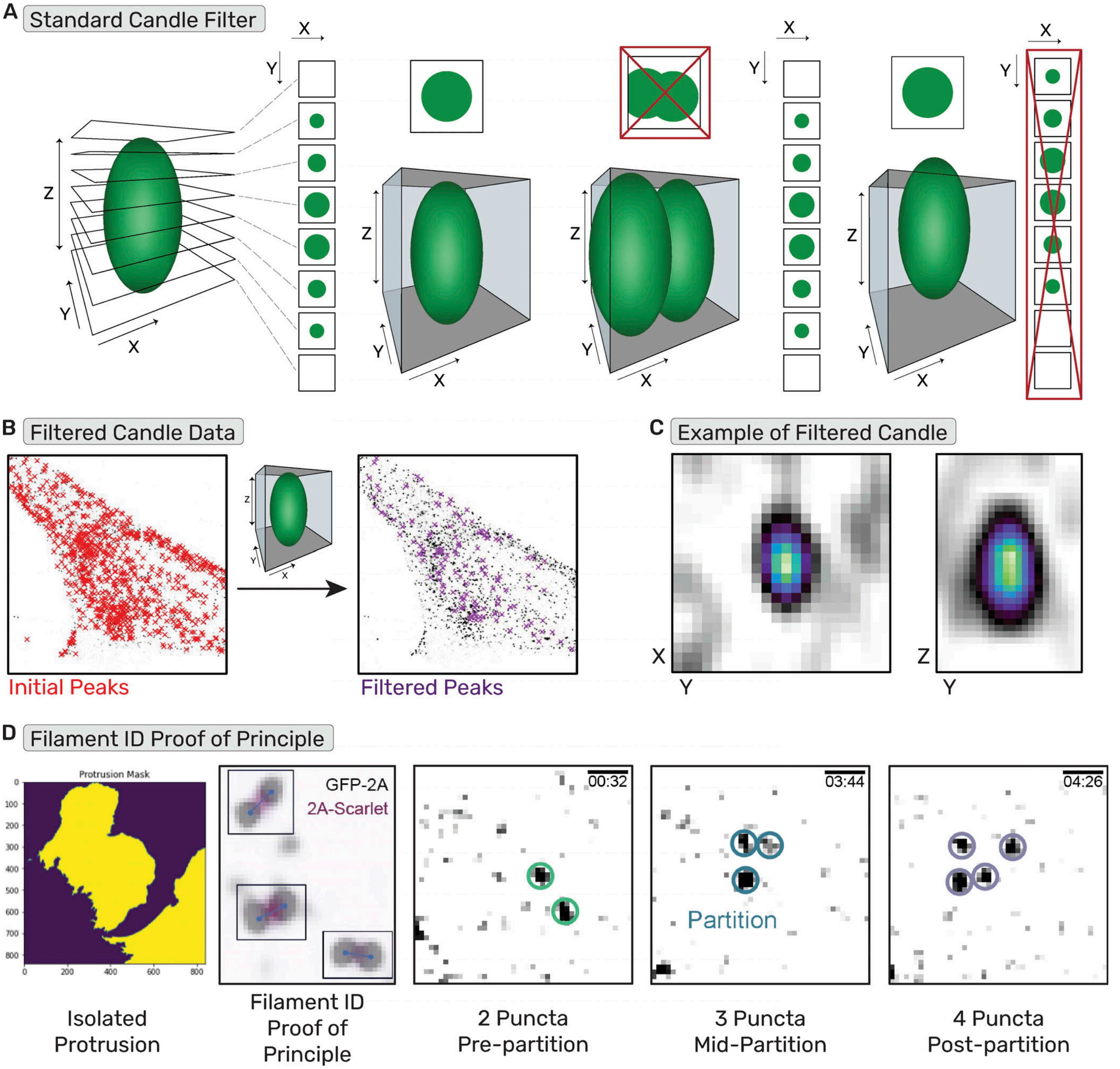

Figure S2. **Molecular counting workflow. (A)** Depiction of the filter used to identify candles unsuitable for analysis (i.e., too close to another candle or partially out of Z-range). **(B)** Example of standard candle image before and after filter. **(C)** Example image of candle deemed passable by the filter in XY and ZY. **(D)** Depiction of NM2 filament identification workflow with (1) lamella isolation, (2) filament identification by puncta ∼300 nm apart with proof of principle NM2-tail tag to confirm filament, and (3) examples of the 2-puncta, 3-puncta, and 4-puncta identifications.

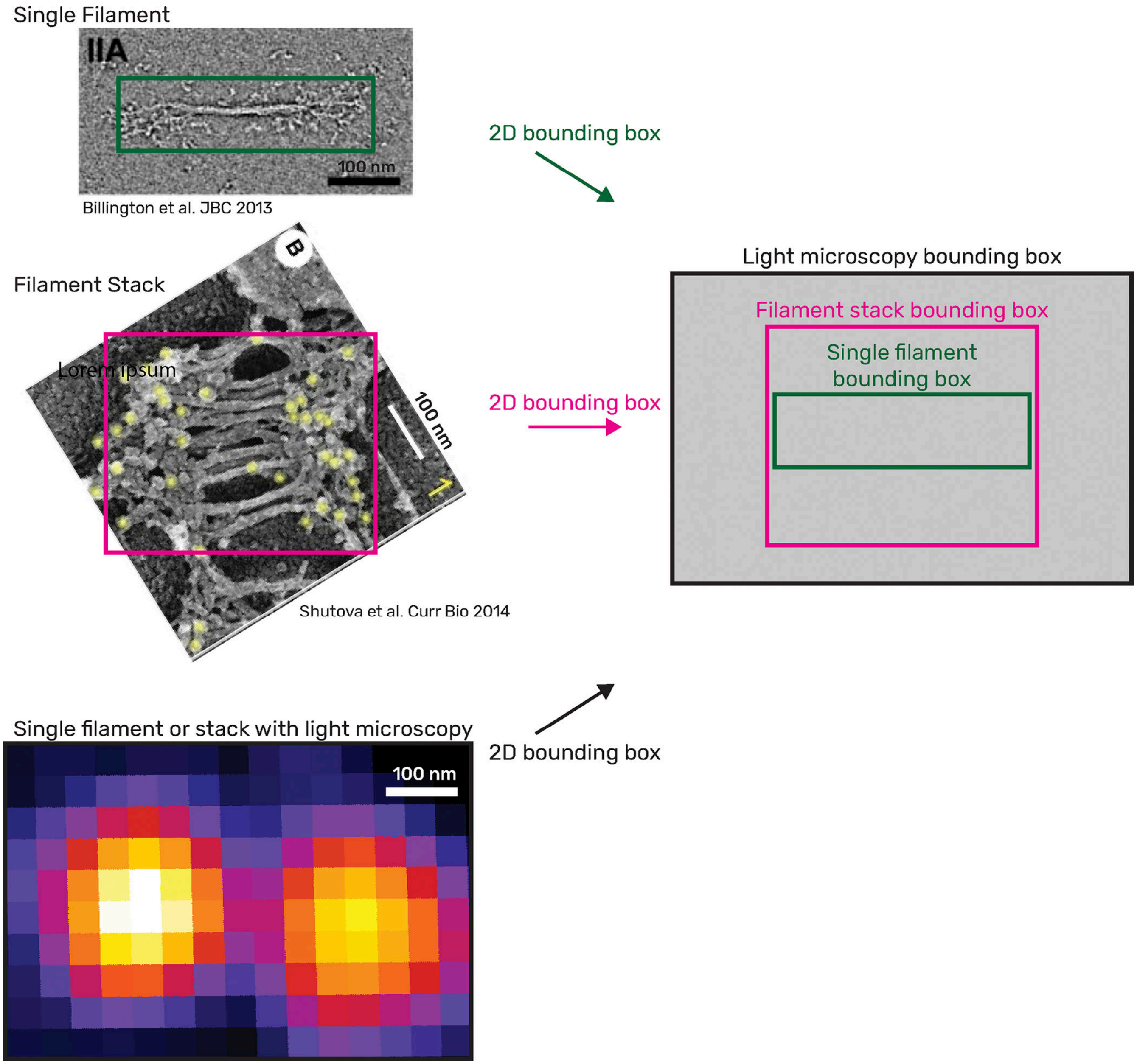

Figure S3. **Filament stacks easily fit in light microscope pixels** The 2D bounding boxes for a single filament (top left; green), a filament stack with ~12 NM2 filaments (middle left; magenta), and a doublet of EGFP-NM2A imaged with high-resolution Airyscan imaging (bottom left; black) were overlayed to demonstrate that many NM2 filaments can fit into the light microscopy pixels used throughout this study, consistent with our molecular counting numbers. These numbers should only increase when considering 3D light microscopy voxels and 3D z-stacks.

Video 1. **NM2 filament appearance tracking.** Sum intensity Z-projection of a time-lapse of an EGFP-NM2A knock-in cell. Lamellar protrusion imaged with a 5-s frame rate. The leading edge is in the top right corner with retrograde flow to the bottom left. Magenta circles mark NM2 filaments in the first frame of appearance. Frame rate = 15 fps. Scale bar = 5 µm. Time = mm:ss.

Video 2. **Leading edge retraction precedes NM2 filament appearance.** Sum intensity Z-projection of time-lapse of EGFP-NM2A knock-in cell. Lamellar protrusion imaged with a 1 s frame rate. The leading edge is in the top right corner with retrograde flow to the bottom left. Frame rate = 15 fps. Scale bar = 5 µm. Time = mm:ss.

Video 3. **JL treatment stalls actin dynamics.** Sum intensity projection of a z-stack time-lapse of 3x-mScarlet-FTractin tagged lamellar protrusion with a 5-s frame rate. The leading edge is in the top right corner with retrograde flow to the bottom left. Frame rate = 30 fps. Scale bar = 5 µm. Time = mm:ss.

Video 4. **DMSO treatment with NM2 appearance.** Sum intensity projection of a z-stack time-lapse of EGFP-NM2A knock-in cell expressing 3x-mScarlet-FTractin. Lamellar protrusion imaged with a 5-s frame rate. The leading edge is in the top right corner with retrograde flow to the bottom left. Actin is in gray LUT, and NM2A is in purple LUT. Drug treatment is indicated in orange text at the first frame of treatment. Frame rate = 20 fps. Scale bar = 5 µm. Time = mm:ss.

Video 5. **JL treatment with NM2 appearance.** Sum intensity projection of a z-stack time-lapse of EGFP-NM2A knock-in cell expressing 3x-mScarlet-FTractin. Lamellar protrusion imaged with a 5-s frame rate. The leading edge is in the top right corner with retrograde flow to the bottom left. Actin is in gray LUT and NM2A in purple LUT. Drug treatment indicated in orange text at the first frame of treatment. Frame rate = 20 fps. Scale bar = 5 µm. Time = mm:ss.

Video 6. **Actomyosin dynamics during long-term cell migration.** EGFP-NM2A knock-in cells expressing 3x-mScarlet-FTractin imaged every minute for 8 h. Actin is in gray LUT and NM2A in purple LUT. Frame rate = 30 fps. Scale bar = 50 µm. Time = hh:mm:ss.

Video 7. **Tail retraction precedes NM2 filament appearances.** Sum intensity projection of a z-stack time-lapse of EGFP-NM2A knock-in cells imaged with a 20-s frame rate. The initial tail outline is in orange, and the initial protrusion outline is in green. Frame rate = 40 fps. Scale bar = 20 µm. Time = mm:ss.

Video 8. **Y27 treatment results in increased NM2 filament appearances.** Time-lapse of EGFP-NM2A knock-in cell with a 5-s frame rate. Drug treatment indicated in orange text at the first frame of treatment. Frame rate = 50 fps. Scale bar = 50 µm. Time = hh:mm.

Video 9. **JLY treatment with NM2 appearance.** Sum intensity projection of a z-stack time-lapse of EGFP-NM2A knock-in cell expressing 3x-mScarlet-FTractin. Lamellar protrusion imaged with a 5-s frame rate. The leading edge is in the top right corner with retrograde flow to the bottom left. Actin is in gray LUT, and NM2A is in purple LUT. Drug treatment is indicated in orange text at the first frame of treatment. Frame rate = 20 fps. Scale bar = 5 µm. Time = mm:ss.

Video 10. **NM2 monomer recruitment jumpstarts NM2 filament assembly.** Sum intensity projection of a z-stack time-lapse of Halo-NM2A knock-in cell expressing GFP-Stargazin-Lov-SsrA and SspB-mApple-NM2A. Lamellar protrusion imaged with a 10-s frame rate. The leading edge is in the top right corner with retrograde flow to the bottom left. Recruitable (SspB-mApple) NM2 is shown in the left panel, endogenous (Halo-NM2) in the middle panel, and an overlay with recruitable in blue and endogenous in purple in the right panel. The orange circle marks the activation ROI that was stimulated after each acquisition frame. Frame rate = 50 fps. Scale bar = 5 µm. Time = mm:ss.

Video 11. **NM2 filament mediated amplification.** Sum intensity projection of a z-stack time-lapse of EGFP-NM2A knock-in cell. Lamellar protrusion imaged with a 5-s frame rate. The leading edge is in the top right corner with retrograde flow to the bottom left. Frame rate = 50 fps. Scale bar = 5 µm. Time = mm:ss.

Video 12. **NM2 filament partitioning.** TIRF-SIM time-lapse of EGFP-NM2A knock-in cell with a 2-s frame rate. Green circles indicate the first frame with 2-puncta ∼300 nm apart or pre-partitioning. Blue circles indicate the first frame with 3-puncta ∼300 nm apart or mid-partitioning. Purple circles indicate the first frame with 4-puncta ∼300 nm apart, or post-partitioning. Frame rate = 12 fps. Scale bar = 300 nm. Time = mm:ss.